A 3D mesoscopic frictional cohesive zone model for the steel-concrete interface

Mohammad Abbas, Benoît Bary, Ludovic Jason

To cite this version:

Mohammad Abbas, Benoît Bary, Ludovic Jason. A 3D mesoscopic frictional cohesive zone model for the steel-concrete interface. International Journal of Mechanical Sciences, 2023, 237 (1), pp.107819. ⟨10.1016/j.ijmecsci.2022.107819⟩. ⟨cea-03851038⟩

HAL Id: cea-03851038

https://cea.hal.science/cea-03851038v1

Submitted on 1 Feb 2026

A 3D mesoscopic frictional cohesive zone model for the steel-concrete interface

Mohammad Abbas [a,*], Benoît Bary [a], Ludovic Jason [b]

[a] Université Paris-Saclay, CEA, Service d'Étude du Comportement des Radionucléides, 91191, Gif-sur-Yvette, France

[b] Université Paris-Saclay, CEA, Service d'Études Mécaniques et Thermiques, 91191, Gif-sur-Yvette, France

Key Words: *3D cohesive zone model; Damage; Friction; Steel-concrete interface; Pull-out test; Smooth and ribbed bars*

ABSTRACT

It is essential to model the behavior of the interfaces between steel reinforcement and concrete in order to understand the stress transfer between these two components in reinforced concrete structures, which strongly affects the initiation and propagation of cracks. The macroscopic interface models commonly used in structure simulations are functions of various parameters whose physical significance is sometimes not very clear and identification is difficult. That is why the mesoscopic scale is investigated here to improve the understanding of the behavior of the interface when considering both ribbed and smooth bars. A 3D interface model is proposed and implemented to this aim. It takes into account friction and damage by combining a modified cohesive zone model (CZM) based on Tvergaard's approach, and a frictional model in the damaged part of the interface. In this contribution, three dimensional numerical reinforced concrete samples, representing pullout tests, are generated with a detailed geometry of the steel bar. Then, pull-out numerical simulations are performed on the generated samples using an isotropic damage approach with regularization in tension and in compression in order to describe cracking in concrete. The interface model is described and its functionality is verified on a pullout test with smooth bar. The overall response is studied in terms of damage and distribution of the principle stresses near the steel bar, and the applied force versus free end displacements curves which are compared to available experimental data. Finally, a good agreement between simulations and experimental results when using smooth and ribbed bars is obtained.

1 INTRODUCTION

Civil Engineering structures do not only aim to sustain external loadings. Their success or failure is neither only evaluated by their simple mechanical resistance nor only dependent on it. For instance, cracking has a direct impact on the transfer properties that govern the potential leakage rate in containment buildings for

---

* Corresponding author.
E-mail addresses: mohammad.abbas@cea.fr (M. Abbas), benoit.bary@cea.fr (B. Bary), ludovic.jason@cea.fr (L. Jason)

nuclear power plants. In some cases, information about the cracking behavior related to the quasi-brittle evolution of concrete can become essential.

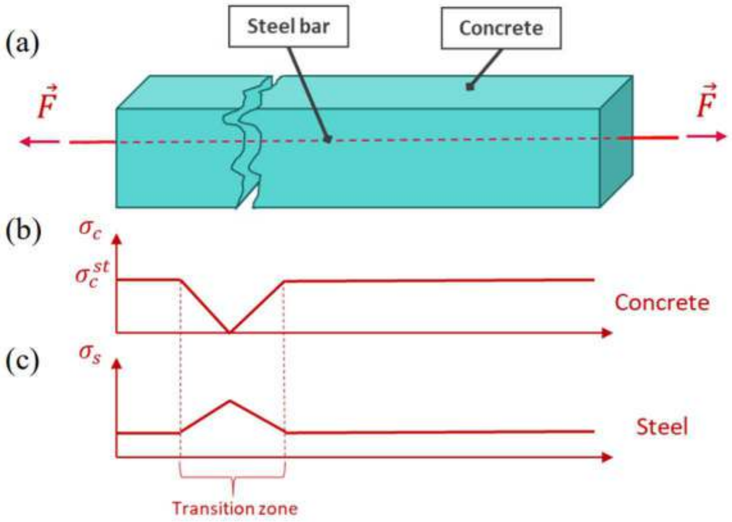

Figure 1. Transfer of stresses in reinforced concrete tie. (a) Concrete tie having an embedded steel bar in its center, under a pulling force $\vec{F}$. Distribution of stresses after the first crack in (b) concrete and (c) steel. σ_c^{st} is the concrete strength, while σ_c and σ_s are the stresses in concrete and steel respectively, based on [1]

The bond between steel and concrete plays an essential role in determining the structural performance of reinforced concrete structures. This steel-concrete interface is very complicated due to the presence of various phenomena at this region. For instance, corrosion of steel, which was studied previously in [2–8], is a crucial phenomenon that affects reinforced concrete structures, by affecting considerably the interface and then the bond, leading to the damage of the concrete cover by the corrosion products. In the case of a reinforced tie for example, once the first crack appears in the weakest point of the structure, the concrete stress in the cracked zone drops to zero while the load is totally supported by the steel reinforcement. The stresses are then progressively transferred from steel to concrete (Figure 1). This transition zone has an impact on the crack properties and is directly influenced by the bond between steel and concrete [1]. Thus, in order to have a good work performance, a sufficient bond property between the steel bars and the surrounding concrete should be considered.

Different scales can be used to model the steel-concrete interface. At the macroscopic level, concrete is modelled as a homogeneous material and the governing equations are formulated within the framework of continuum mechanics, which is done in e.g. [1,9–13]. At another level, the mesoscale analysis can reveal the local responses of concrete and reinforcement and their interactions with cracking. It aims to capture the behavior at the scale of the ribs of the steel bar. Different methods are available to represent the concrete numerically at the mesoscopic scale. In most of the mesoscopic models, the concrete is subdivided into matrix and coarse aggregates such as [5,14–20], while some mesoscopic models have considered concrete as a homogeneous material like in [21–26]; still, the detailed geometry of the ribs was modelled in order to consider the complex geometry of the bond at this scale. The mesoscopic representation was adopted using discrete element methods like in [21,22,26–28] and also using continuum finite element methods like in [15,16,23–25].

According to [29,30], the ribbed steel bars and concrete interaction phenomena can be divided into three parts: the cementing force between the steel bar and concrete, which has a little effect, the friction between the two surfaces, and geometrical interlock. More precisely, the bond strength for smooth and ribbed bars depends mainly on friction and mechanical or geometrical interactions [29]. Due to the complexity of the steel-concrete zone, different approaches have been used to represent the steel-concrete interface. In studies like [21,22,26,31], it was represented by an interfacial transition zone (ITZ) between concrete and steel, which affected the initiation and propagation of cracks. On the other hand, zero-thickness elements were used in [32,33], in which the surface of contact between concrete and steel represented the interface, while a contact friction was recently deployed in [23–25] to simulate the steel-concrete bond without using any interface elements. In such zero-thickness approaches, which is going to be used in this study, friction can be applied directly to the surface of contact, along with other phenomena that are a direct reflection of properties of concrete, thus combining both concrete properties and contact friction between the two surfaces.

The cohesive zone model was first early developed and introduced by [34,35].The former suggested that in the zone ahead of slits in steel plates, which are subjected to a static tension load, the stress in this zone is constant and equal to the yield strength of the material. On the contrary, the latter pointed out that the stresses in this softening region were variable. Since then, the cohesive zone model has been applied to predict failure in various materials, such as composites [36] and concrete [37]. Theoretically, such approach describes the failure of the material by introducing a strength-based fracture criterion along with an energy based fracture criterion for the part ahead of the crack tip. The cohesive zone elements are embedded along the fracture plane, which deforms according to a traction–separation law that takes into account the appropriate strength and toughness [38]. Such models gave good solutions when assigned to aggregates-mortar interface [19], fiber reinforced polymer FRP-steel joints [39], FRP-concrete interface [40]. It has been recently assigned to retarded-bonded tendons and concrete interface in [41], encouraging its introduction to steel-concrete interfaces at the mesoscopic scale.

A different approach was initially proposed by [42] as a 2D model, in which the cohesive crack propagation phenomena, which is governed by nonlinear fracture mechanics, can be modelled at a meso-mechanical level by assuming that a representative elementary area A of the interface can be decomposed into an undamaged part and a completely damaged part. This 2D model, which was extended in [33,43,44] to a 3D approach, is able to capture crack initiation, damage propagation and their coupling with friction, interlocking and associated dilation. It was generalized to 3D in [45–47]. In these formulations, damage evolves based on Crisfield’s bilinear damage model presented in [48], while the frictional behavior is governed by a Coulomb’s law. This approach was used once to study steel-concrete interface in [33] in 2D, still the smooth bar post-peak behavior produced was linear, which is due to the Crisfield’s damage model chosen. Recently, [49] used this 2D model to represent the contact between timber and concrete by varying friction coefficient.

Although some existing steel-concrete interface models are able to reproduce the overall behavior of the pull-out tests, they mainly succeed when using a sample with ribbed bar. However, such models cannot in general easily capture the overall behavior when using a smooth bar. As smooth bar behavior may be seen as an initial step to capture the more complex ribbed bar behavior, it is believed that a comprehensive model should be able to reproduce the response of both bar types. For example, contact friction formulation used recently in [7,8,23–25] has proved to be well-adapted to 3D approach, and has been further used in different related studies [50,51]. Nonetheless, it seems not able to reproduce efficiently the response of concrete-steel bond with smooth bar. Additionally, such formulations have a big cost in terms of computational time [52] when used with even more finer meshes compared to [7,8,23–25]. In order to analyze results locally at a very small scale near each rib, there is a clear interest to use a different approach. Likewise, the 3D frictional approach used recently in [53] possesses a similar difficulty when applied on large meshes.

The steel-concrete interfacial region, where friction plays an essential role, is still a continuation of the surrounding concrete. Hence, cracks will propagate in concrete starting from the surface that is in direct contact with the steel bar. Similar to the cracking in concrete volume, the cracks at the interface can be represented by a damage parameter, which has not been combined with friction in previous steel-concrete interface models.

The aim of this work is to develop an interface model to represent the steel-concrete interface at the mesoscopic scale and to study its effect by running pull-out test simulations on numerically generated samples, then to compare their response to experimental results. This model is expected to improve the understanding and the prediction of the mesoscopic steel-concrete interface behavior in various configurations and loading conditions. Ultimately, the model will be used to help calibrating a macroscopic simplified interface model developed for structure simulations, whose parameters identification would necessitate a complex experimental procedure. In this regard, the developed model is not intended to be applied at the structure level. Rather, fine meshes are applied on the small numerical samples, in order to study the response locally at the mesoscopic scale. The newly implemented frictional cohesive zone model combines a modified Tvergaard’s approach initially presented in [54,55], and Coulomb’s simple friction. It should be versatile enough to capture the macroscopic behavior of the pull-out test when using either ribbed or smooth bars. Concrete 3D samples are generated, involving the detailed geometry of the ribs explicitly taken into account, and considering homogenous concrete surrounding the bar for simplicity. These pull-out test simulations are first performed on the sample having smooth bar, in order to study the applicability of the new model, and then on the more complicated spiral-ribbed case. The numerical responses in terms of mean bond stress versus free end displacement are compared to available experimental data. The propagation of damage and the principle stresses and strains that develop in the concrete and the interfaces are analyzed locally to highlight their role in the bond behavior.

2 DESCRIPTION OF PULL-OUT TEST SIMULATIONS

In this part, the geometrical description of the pull-out test is given, followed by the description of the behaviors assigned for concrete and steel in the pull-out test simulations. Specifically, concrete is assigned the damage Mazars model with a regularization method in both tension and compression, in order to prevent mesh dependency.

2.1 Description of the pull-out test

According to RILEM recommendations [56], the steel-concrete bond can be characterized by pull-out tests. This test consists in the direct wrenching of a steel bar from a concrete specimen: a bar incorporated in a concrete cube with a defined length is strained at one end by a tensile force, the other end remaining without stress. The tensile force and the relative displacement between steel and concrete are measured. The load is increased up to failure of the adhesion [57]. In this contribution, a three-dimensional mesoscale finite element model is established in order to study the steel-concrete bond.

According to [57], the test specimen is a cube of concrete and the bar is incorporated in its axis. The effective embedment height of the bar corresponds only to the half-height of the specimen. In the other half there is no adhesion between the bar and the concrete. This is in order to reduce the influence of the disturbed area that forms close to the bearing plate. The bar to be tested extends beyond the two sides of the specimen; the tension is applied to the longer end, and the device for measuring the displacement, called FED in this work, between steel and concrete is set on the shorter end. The height of the concrete specimen is 10d with d as the diameter of the bar. Encasement height is 5d and pre-length is 5d (without adhesion).The length of the sides of the concrete specimen is 10d (Figure 2).

2.2 Generation of pull-out test numerical sample

The geometry of the samples is generated using the geometry module of the integration platform for numerical simulations Salome [58]. The cubic sample is composed of two different phases; a smooth steel bar embedded in the central axis of the sample and homogeneous concrete surrounding the steel bar.

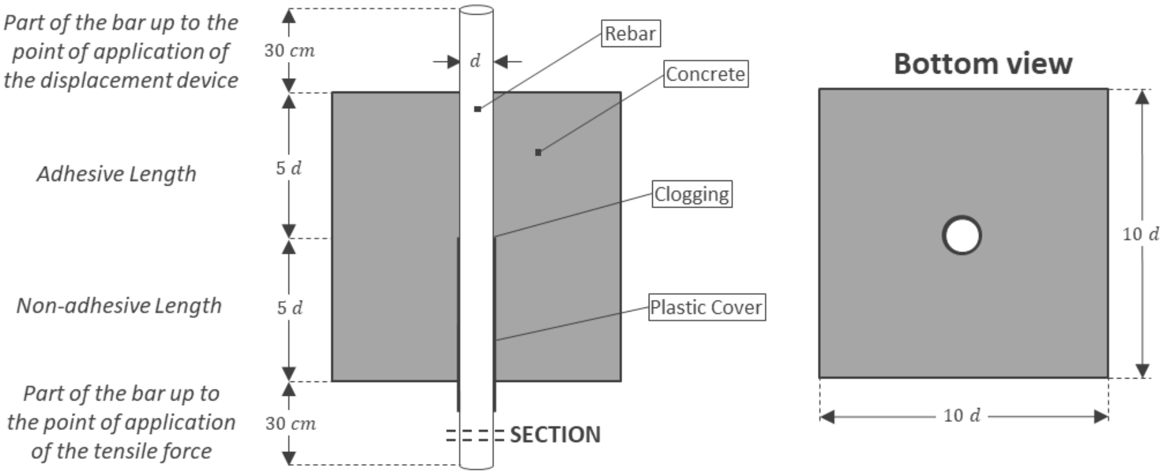

Figure 2. Description and dimensions of the pull-out test piece, formed of a steel bar embedded in the center of a concrete cube, based on [57]

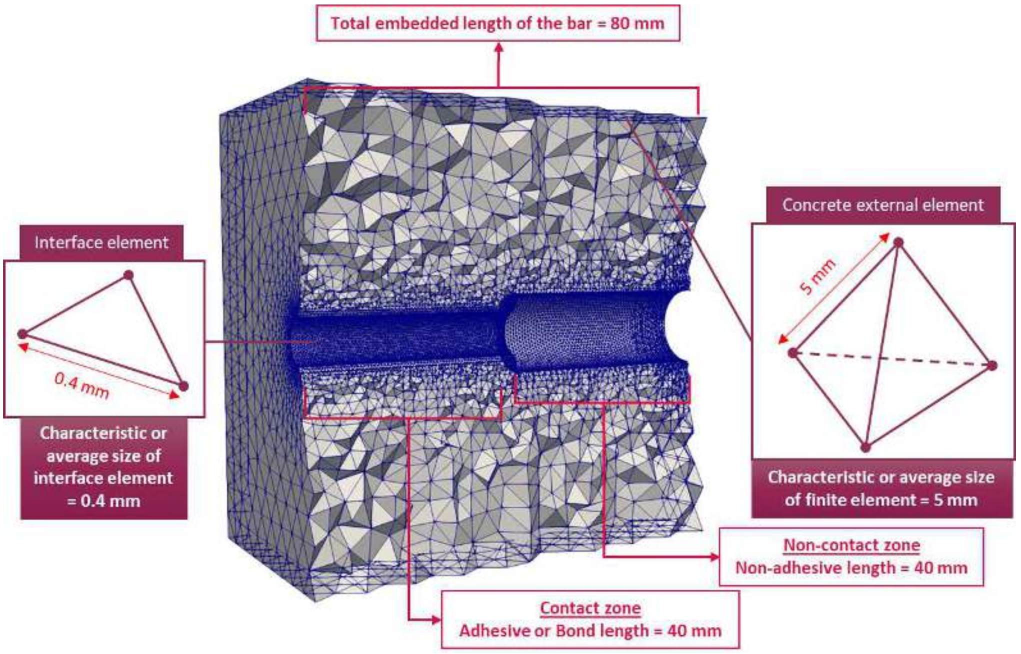

Figure 3 Concrete meshed section, showing the total embedded length of the bar that is divided into contact and non-contact zones, and the characteristic or average size of the sides of the interface surface element and the concrete external tetrahedral elements.

The diameter d of the bar is taken equal to 8 mm, and the cubic sample length is 80 mm, which is in accordance with the recommended pull-out test. In addition, the embedded length of the steel bar is also 80 mm, divided equally into adhesive and non-adhesive lengths as shown in Figure 3.

The meshing is carried out on the generated sample geometry, using the meshing software plugged to the platform Salome. An unstructured mesh is applied using linear tetrahedral meshing elements. The number of mesh elements in the concrete is 303 000 while the number of mesh elements in the steel bar is 310 000 for the smooth sample case. The characteristic size of each mesh element at the outer surface of the concrete sample is equal to about 5 mm, while the triangular edge of each element at the steel concrete interface is almost 0.4 mm (Figure 3). In addition, the interface elements are surface elements with a zero thickness.

2.3 Materials models and parameters of concrete

The type of microstructural evolution in concrete mainly depends on the stress state. The cracking can be dealt with by Continuum Damage Mechanics (CDM), which is based on the progressive reduction of the material stiffness in the framework of continuum mechanics. As commonly done when using damage mechanics, in this contribution, a “crack” is considered when the element is fully damaged. For example, when D=1, the element is fully damage and the stress is near to zero.

In here, Mazars classical model [59] is considered, which is the most widely used damage model for geomaterials such as concrete. This model is able to reproduce the direct cracking under both tensile and compressive stresses (or strains). Mazars classical model [59] is as follows:

Constitutive law:

$$\sigma_{ij} = (1 - D)C_{ijkl}\varepsilon_{kl} \tag{1}$$

where σ is the stress tensor, ε is the strain tensor, D is the total damage and C is the stiffness tensor. The criterion for damage evolution reads:

$$f(\varepsilon_{eq}, D) = \varepsilon_{eq} - \kappa(D) \tag{2}$$

where the threshold of damage growth $\kappa(D)$ and the equivalent strain ε_{eq} are written as:

$$\kappa(D) = \max_{history} \varepsilon_{eq} \quad \text{and} \quad \varepsilon_{eq} = \sqrt{\sum_{i=1}^{3} \langle \varepsilon_i \rangle_+^2} \tag{3}$$

and the initial value of $\kappa(0) = \varepsilon_{D_0}$, where ε_{D_0} is the initial damage threshold. Also, $\langle \cdot \rangle_+$ represents the positive part of the principle strains ε_i . In order to emphasize the unsymmetrical behavior between tensile and compressive states of stresses, the total damage D is a linear combination of damage in tension D_t and in compression D_c following:

$$D = \alpha_t^{\beta} D_t + \alpha_c^{\beta} D_c \tag{4}$$

D_t and D_c have their own evolution law:

$$D_{t,c} = 1 - \frac{\varepsilon_{D_0}\left(1 - A_{t,c}\right)}{\varepsilon_{eq}} - \frac{A_{t,c}}{\exp\left(B_{t,c}\left(\varepsilon_{eq} - \varepsilon_{D_0}\right)\right)} \tag{5}$$

where $\alpha_c = 1 - \alpha_t$, and α_t is computed from the strain and stress tensors such as:

$$\alpha_t = \sum_{i=1}^{3} \frac{\langle \varepsilon_{ti} \rangle \, \langle \varepsilon \rangle_+}{\varepsilon_{eq}^2} \tag{6}$$

where ε_{ti} are the principal values of the strain tensor due to traction (positive) stress, defined as follows:

$$\varepsilon_t = \frac{1 + v}{E} \sigma^+ - \frac{v}{E} tr(\sigma^+) \tag{7}$$

with the following partition for the stress tensor:

$$\sigma = \sigma^+ + \sigma^- \tag{8}$$

where σ^+ is the tensor containing the positive principal stresses and zero elsewhere, while σ^- is the tensor containing the negative principal stresses and zero elsewhere. ε_{D_0} defines the initial damage threshold and thus through the Young's modulus the tensile strength, A_t the residual stress and B_t the descending slope after the peak. In addition, β is a variable for correction of the shear in order not to neglect the effect of shearing, which will be underestimated if it is taken equal to 1.

According to [60], softening models, such as Mazars damage model, leads to a strong dependency of the cracking energy on the mesh size, in which a strain localization occurs in a certain group of elements redirecting the behavior in the structure. Thus, less energy is dissipated in the structure in such models when the mesh size is small, which can be seen in Figure 4(a). To prevent such effect, a regularization method is used based on Hillerborg concept of fracture energy [60]. The evolution proposed is an exponential evolution [61], in which the damage due to tension D_t is calculated as follows:

$$D_t = 1 - \frac{\varepsilon_{D_0}}{\varepsilon_{eq}} \exp\left(B_t\left(\varepsilon_{D_0} - \varepsilon_{eq}\right)\right) \tag{9}$$

while B_t is calculated as follows:

$$B_t = \frac{l \cdot E \cdot \varepsilon_{eq}}{G_f - \frac{l \cdot \varepsilon_{eq}^2}{2E}} \tag{10}$$

where l is the characteristic size of the finite element, G_f is the fracture energy and E is concrete's Young modulus. Thus, the value of B_t assigned in the pull-out simulations is unique to each finite element. The behavior for 2 element sizes can be seen in Figure 4(b). The characteristic size l is calculated as follows:

$$l = \sqrt[3]{\frac{12V}{\sqrt{2}}} \tag{11}$$

where V is the volume of the finite tetrahedral element.

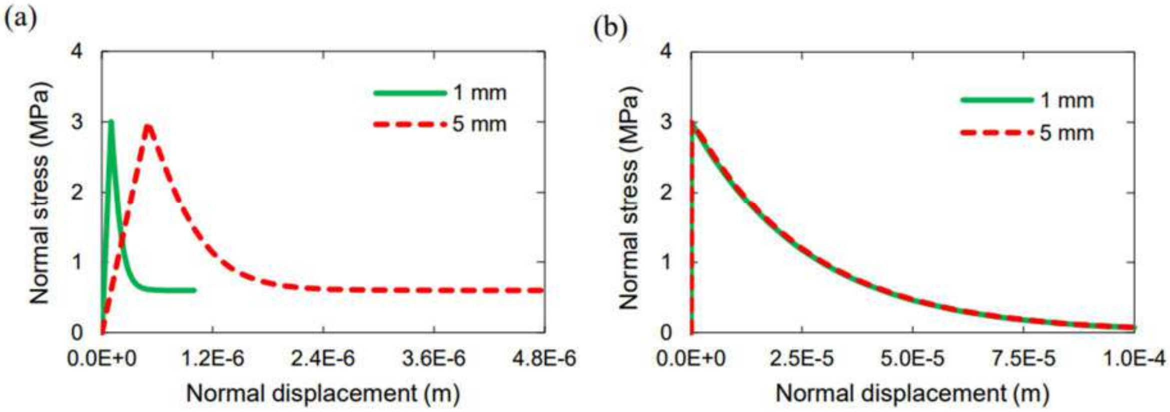

Figure 4. Stress - displacement response under uniaxial tension on two concrete finite elements whose sizes are 1 mm and 5 mm of: (a) the classical Mazars model using $A_t = 0.8$, $B_t = 17000$ and $f_t = 3\ MPa$ and (b) the regularized Mazars using $G_f = 80\ N/m$ and $f_t = 3\ MPa$

Table 1. Mazars parameters A_c and B_c assigned for different element sizes

$l(in\ mm)$	A_c	B_c
0.2	0.0033	5.8

1	0.0169	29.6
2	0.0343	60.3
3	0.0517	90
5	0.09	152

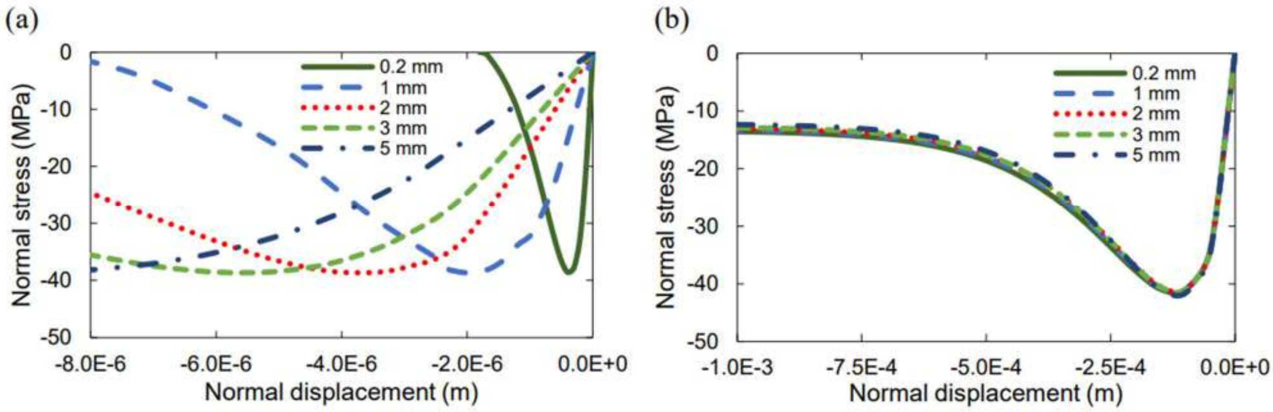

Figure 5. Stress - displacement response of Mazars model under compression on five concrete finite elements whose sizes are given using: (a) common values $A_c = 1.4$, $B_c = 1900$; (b) values of A_c and B_c depending on the element size (see Table 1)

Additionally, [62] showed that the stress-strain curve in compression is influenced by the slenderness of the specimen, unlike the stress-displacement curve, which was also found in different experimental results like [63,64]. Thus, just like in tension, numerical behavior in compression should be also independent of the size of the mesh elements. This justifies the need to develop a methodology for regularizing the compressive behavior of concrete. Hence, a similar problem occurs under compression when assigning A_c and B_c the values recommended by [65], because the sizes of the finite elements may be very small. This effect can be seen in Figure 5(a) plotting the stress-displacement curves for different sizes of element. The values of the parameters A_c and B_c are varied for each case until reaching a very similar general behavior, following the methodology from [66]. These chosen values of A_c and B_c that best fit are shown in Table 1, and the corresponding behavior can be seen in Figure 5(b).

Finally, an evolution law for each of these two parameters is eventually used by using a second-degree polynomial as follows:

$$A_c = -335.9133\, l^2 + 16.2746\, l - 0.0002 \tag{12}$$

$$B_c = 140984.5429\, l^2 + 29701.4423\, l - 0.0996 \tag{13}$$

Regarding the other parameters of the concrete model, the values assigned in the pull-out simulations for the initial damage threshold is $\varepsilon_{D_0} = 10^{-4}$ and the shear correction coefficient is $= 1.06$. In addition, concrete's Young's modulus E_{con} and fracture energy $G_{f\,con}$ in tension are adapted to the experimental properties provided for each simulated case, while concrete's Poisson's ratio is set to 0.2 in all the simulations.

On the other hand, the steel bar is assigned an elastic model, where its Young's modulus is 200 GPa and its Poisson's ratio is 0.3. The yield stress limit is 365 MPa, which is not be exceeded, and if so a perfect yield behavior is used after which the Von Mises stress will always be equal to the yield stress as the steel is strained.

The last component of the simulation is the interface model, which is discussed in details in the following section.

3 FRICTIONAL COHESIVE ZONE INTERFACE MODEL

The development of a frictional cohesive zone interface model (FCZM) is mainly motivated by the fact that the pull out test response with smooth bar cannot easily be reached with standard interface models. To illustrate this point, two classical models, namely Tvergaard's cohesive zone model and Coulomb's interface model (see Appendices for a detailed description), are assigned separately to the steel-concrete interface pull-out test simulations using a smooth bar with acceptable range of model parameters. The numerical results are compared to the experimental data extracted from [67] in terms of mean bond stress versus free end displacement in Figure 6. The mean bond stress σ_{mb} is calculated as follows:

$$\sigma_{mb} = \frac{F}{\pi \cdot d \cdot l} \tag{14}$$

where F is the applied force, d is the mean diameter of the steel bar and l is the adhesive length of the steel.

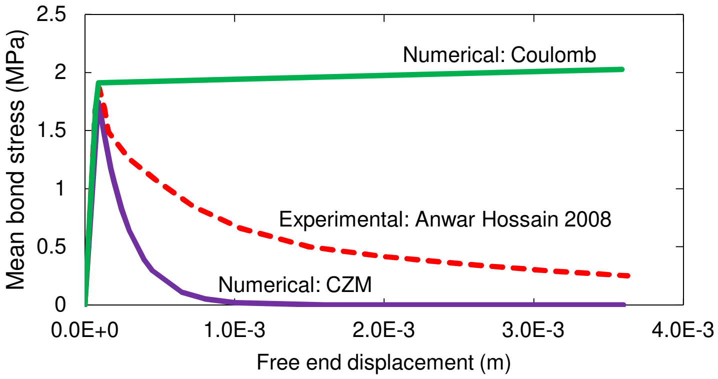

Figure 6. Mean bond stress versus free end displacement of the two simulations using the CZM and Coulomb's interface model, compared to the experimental results shown in [67]

One can see the inability of Tvergaard's cohesive zone model and Coulomb's interface model to reproduce accurately the experimental behavior. For the CZM, one disadvantage in this case is the non-existence of any effect of compression on the shearing phenomenon, which leads always to zero residual stress. Still, an important advantage is the non-linear decay of stress and the usage of damage to represent the cracking in the interface, which is viewed, as stated before, as a continuation of the surrounding concrete. On the other hand, an advantage of Coulomb's interface model is the constant none zero residual stress observed. However, this model does not contain damage and the residual stress is always equal to the peak stress. Thus, due to the limitations and inability of the two models to reproduce correctly the behavior separately, a combination of both models is proposed in order to take into account their respective advantages.

3.1 Description and formulation

The combination of the elastoplastic and damage-based cohesive approaches is based mainly on what was initially proposed by [42] as a 2D model. According to [42], the cohesive crack propagation phenomena, which are governed by nonlinear fracture mechanics, can be modelled at a meso-mechanical level by assuming that a representative elementary area A of the interface can be decomposed into an undamaged part $(1 - D_{int})A$ and a completely damaged part $D_{int}A$, with the damage parameter D_{int} being the relative measure of the damaged part (Figure 7).

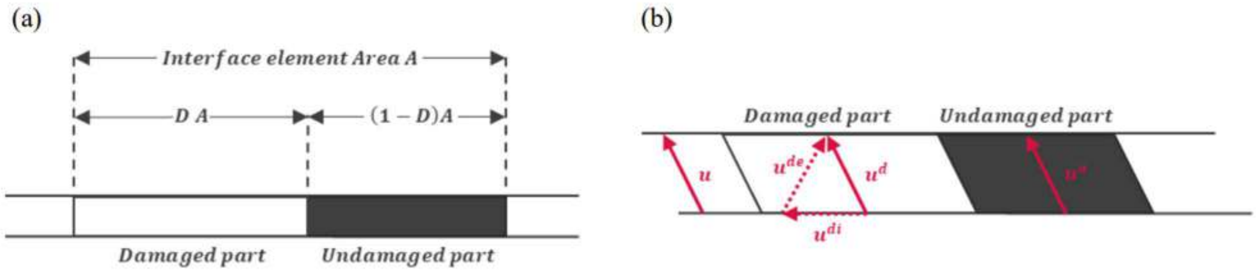

Figure 7. Meso-mechanical interpretation of the frictional cohesive interface model. It shows (a) the decomposition of the representative interface element and (b) the kinematic assumptions, based on [42]

In this model, which was generalized to a 3D approach in [45–47], damage evolves based on Crisfield's bilinear damage model presented in [48], while the frictional behavior is governed by a Coulomb's law. Recently, [49] used this 2D model to represent the contact between timber and concrete by varying friction coefficient.

Here, the approach initially proposed in [42,45] is extended by using the Tvergaard's cohesive zone model, along with certain modifications in compression to maintain continuity of stress when there is a sudden change in the type of stress, for describing the undamaged stress at the interface. In contrary to Crisfield's model, Tvergaard's CZM is adopted due to its more realistic post-peak behavior, and to prevent reaching a null stress, which may lead to some numerical problems.

The new proposed model is implemented using the open source MFront code generator [68], then it has been imported to the finite element code Cast3M [61] to perform the pull-out test simulations.

Similarly to [42], the element is divided into an undamaged part A_u, where the interface is fully bonded, and a damaged part A_d, where frictional contact takes place. This can be written as shown in Figure 7, where A is the area and D_{int} is the damage parameter of the interface element. In addition, the relative displacement u is assumed completely constant over the whole interface element, and the relative displacement in the damaged part u^d is divided into an elastic displacement $u^{de}$and an inelastic displacement u^{di} in the tangential direction only, since there is no contact in this part under tension. Moreover, the relative displacement of the undamaged part u^u is assumed to be fully elastic and equal to the elastic displacement of the undamaged part u^{ue}. The interface total stress σ is supposed to be constant on each part. The stress on the undamaged part of the interface is denoted by σ^u, while the stress on the damaged part is denoted by σ^d.

Total stress σ:

The total stress σ is calculated according to the following additive formula:

$$\sigma = D_{int}\sigma^d + (1 - D_{int})\sigma^u \tag{15}$$

Damaged part stress σ^d:

Using a formulation without tension, the stress of the damaged part of the interface σ^d is related to the elastic displacement u^{de} as follows:

$$\sigma^d = Hu^{de} = H(u\text{-}u^{di}) \tag{16}$$

where H is defined as:

$$H = diag\left[\left(1 - v(u_n - u_n^{di})\right)K_n, K_s, K_s\right] = \begin{pmatrix} \left(1 - v(u_n)\right)K_n & 0 & 0 \\ 0 & K_s & 0 \\ 0 & 0 & K_s \end{pmatrix} \tag{17}$$

since $\mathrm{u_n^{di}}$ is always null, and v is the Heaviside function defined as:

$$v(x) = \begin{cases} 0 \; if \; x < 0 \\ 1 \; if \; x \geq 0 \end{cases} \tag{18}$$

K_n is the normal stiffness and K_s is the shear stiffness.

Thus, the term $(1 - v(u_n))$ is null when $u_n \geq 0$, because it is a no tension relation by definition, and it is equal to 1 when $u_n < 0$, representing the compressive behavior.

The inelastic displacement u^{di} represents the inelastic sliding that has occurred on the damaged part of the interface element. It is described in the framework of non-associated elastoplasticity as in [42] and [69] by introducing a Coulomb yield friction function $\zeta(\sigma^d)$:

$$\zeta(\sigma^d) = \mu \cdot \langle\sigma_{dn}\rangle_- + \sqrt{(\sigma_{dt})^2 + (\sigma_{dh})^2} = \mu \cdot \sigma_{dn} + \sqrt{(\sigma_{dt})^2 + (\sigma_{dh})^2} \tag{19}$$

where σ_{dn} is the normal stress in the damaged part and σ_{dt} and σ_{dh} are the corresponding shear stresses in the two tangential directions t and h. μ is the friction coefficient and $\langle\cdot\rangle_-$ represents the negative part of the stress. The second equation is always true since σ_{dn} is always negative in accordance with Eqs. (16), (17) and (18) .

The evolution of $\dot{u}^{di}$ is controlled by a non-associative relationship expressed using a nonnegative plastic multiplier ω, which is a common choice in computational inelasticity [69], according to the formula:

$$\dot{u}^{di} = \dot{\omega}\begin{pmatrix} 0 \\ \dfrac{\sigma_{dt}}{\sqrt{(\sigma_{dt})^2 + (\sigma_{dh})^2}} \\ \dfrac{\sigma_{dh}}{\sqrt{(\sigma_{dt})^2 + (\sigma_{dh})^2}} \end{pmatrix} \tag{20}$$

and by considering Kuhn–Tucker conditions [70] and in order to take into account the irreversible nature of frictional sliding:

$$\begin{cases} \dot{\omega} \geq 0 & (1) \\ \zeta(\sigma^d) \leq 0 & (2) \\ \dot{\omega}\,\zeta(\sigma^d) = 0 & (3) \end{cases} \tag{21}$$

By using Eqs.(20) and (21), the inelastic displacement u^{di} can be calculated.

<u>Undamaged part stress σ^u:</u>

Unlike [42,45] which used the Crisfield's bilinear model initially proposed in [71] and modified in [48,72], Tvergaard's cohesive zone model is implemented to represent the stress in the undamaged part of the interface, with some additional modifications applied in order to take into account the exponential behavior, especially under compression. On contrary to Crisfield's model where the damage evolution is linear, Tvergaard's model has an exponential evolution that is believed to be more realistic in particular in the smooth bar case which reflects the evolution of the interface model, as previously seen. In addition, as mentioned no zero stress is reached finally, which prevents the occurrence of convergence problems in the numerical solving process.

The non-dimensional parameter λ representing the equivalent opening of the interface is defined according to Eq. (A.2) and the stiffness ratio δ_s is defined according to Eq. (A.3). The damage indicator $\widetilde{\lambda}$ is also calculated based on Eq. (A.4), while the damage variable D_{int} is determined as follow:

$$D_{int} = 1 - \exp\left(\frac{-f_t\,\widetilde{\lambda}}{\varsigma\, G_f}\right) \tag{22}$$

where ς is a non-zero coefficient to be assigned, f_t is the maximum tensile strength of the interface and G_f is the fracture energy.

In addition, the normal stiffness K_n is defined according to Eq. (A.7).

The undamaged part stress σ^u is calculated based on the following equation:

$$\sigma^u = \Gamma K u$$

$$\sigma^u = \begin{pmatrix} \sigma_{un} \\ \sigma_{ut} \\ \sigma_{uh} \end{pmatrix} \;\; ; \;\; \Gamma = (\beta \quad \alpha \quad \alpha) \;\; ; \;\; K = \begin{pmatrix} K_n & 0 & 0 \\ 0 & K_s & 0 \\ 0 & 0 & K_s \end{pmatrix} \;\; ; \;\; u = \begin{pmatrix} u_n \\ u_t \\ u_h \end{pmatrix} \tag{23}$$

This can be simplified as:

$$\begin{cases} \sigma_{un} = \beta K_n u_n \\ \sigma_{us} = \alpha K_s u_s \end{cases} \tag{24}$$

where s represents the two tangential directions t and h.

The two coefficients α and β are introduced in order to reflect the damaged and non-damaged cases, and to try to represent a more logical behavior of the shear stress under compression. In Tvergaard's modified cohesive zone model, shearing with initial compression case is the same as the pure shearing case. Here instead, it is modified to produce a stiffer response when compression is applied, which seems realistic since a higher effort is always needed to shear when this certain surface is under compression.

The coefficient β is defined as follows:

$$\begin{cases} \beta = 1 & For\;\; D = 0 \;\; and \;\; \forall \;\; \sigma_{dn} \\ \beta = \dfrac{\lambda_0}{\lambda} & For\;\; D \neq 0 \;\; and \;\; \sigma_{dn} \geq 0 \\ \beta = \exp\left(\dfrac{f_t\,\widetilde{\lambda}}{\varsigma\, G_f}\right) & For\;\; D \neq 0 \;\; and \;\; 0 \geq \sigma_{dn} \end{cases} \tag{25}$$

while the coefficient α is defined as follows:

$$\begin{cases} \alpha = 1 & For\;\; D = 0 \;\; and \;\; \forall \;\; \sigma_{dn} \\ \alpha = \dfrac{\lambda_0}{\lambda} & For\;\; D \neq 0 \;\; and \;\; \sigma_{dn} \geq 0 \\ \alpha = \dfrac{\frac{\lambda_0}{\lambda} + D - 1}{\gamma}\sigma_{dn} + \dfrac{\lambda_0}{\lambda} & For\;\; D \neq 0 \;\; and \;\; 0 \geq \sigma_{dn} \geq \gamma \\ \alpha = 1 - D = \exp\left(\dfrac{-f_t\,\widetilde{\lambda}}{\varsigma\, G_f}\right) & For\; D \neq 0 \;\; and \;\; \gamma \geq \sigma_{dn} \end{cases} \tag{26}$$

where σ_{dn} is the normal stress in the damaged part of the interface that is calculated using Eqs. (16) and (17). γ is a stress value, taken as -1 MPa in here, but it can be changed. It is a small value chosen in order to maintain continuity of stress when the displacement changes from positive to negative or the opposite, preventing any kind of sudden drop in stress and preserving the smooth continuity of stress.

Note that the three values of β are introduced so that the term $(1 - D_{int})\sigma_{un}$ is equal to Tvergaard's normal stresses σ_n defined in Eqs. (A.6) and (A.10) when $\varsigma = 1$. On the other hand, the first two values of α in Eq.(26) are also chosen so that the term $(1 - D_{int})\sigma_{us}$ is equal to the Tvergaard's shear stresses σ_s defined in Eqs. (A.8) and (A.11), except when the element is under normal compressive stress. Here, the proposed modification to Tvergaard's σ_s is in the fourth value, which gives a stiffer response when there exists a compressive stress. In addition, the third value is assigned in order to maintain continuity between the second and the fourth case, when there is a change in the direction of the displacements, to prevent a sudden drop in stress.

3.2 Validation of the implementation

In order to verify the implementation of the FCZM, several simulations are performed on one interface element connecting two blocks to each other (Figure 8), whose side length is 1 mm, in order to observe the interface element behavior under different loading conditions. A certain shearing or normal displacement is applied either in compression or in tension and the corresponding applied force is calculated. The values assigned to the parameters of the FCZM are shown in Table 2. Additionally, the coefficient ς defined in Eq. (22) is taken equal to 1.

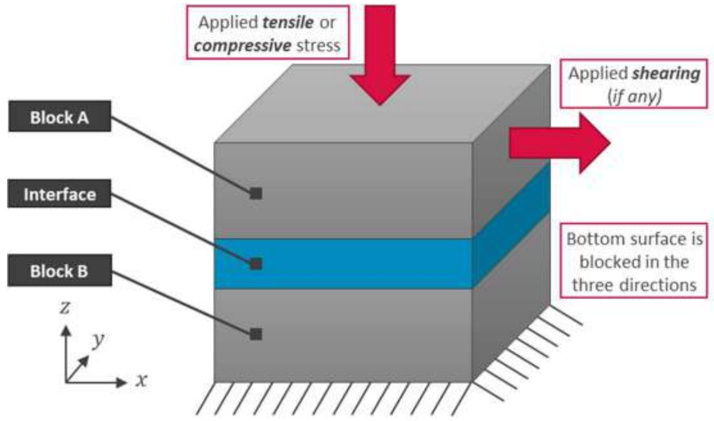

Figure 8. Geometric model for the one-interface element simulations; the side dimension of the zero thickness interface element is 1 mm

Comparing the CZM and FCZM in Figure 9(a), one can see that the behavior in tension reflects purely the behavior of the Tvergaard's model, and so does the behavior in compression. Obviously, friction in pure tension or compression plays no role. The tangential behavior is also investigated by performing several simulations on the same interface element. A certain normal stress, either tension or compression, is initially imposed then a tangential displacement is applied. The corresponding tangential displacements and applied forces are plotted in Figure 9(b) and Figure 9(c). Similarly to the tensile case, the pure shear case shown in Figure 9(b) reflects Tvergaard's model response, including when a certain tensile stress is initially imposed.

Table 2. Assigned values to the parameters of the FCZM in the one-interface element simulations

δ_s	$f_t\ (MPa)$	$G_f\ (N/m)$	$\lambda_0(m)$	μ
1	3	300	2e-5	0.4

To sum up, one can see that in case of pure tension, pure compression, and pure shear and shearing with initial tension, friction has no role, and Tvergaard's modified model is entirely reflected by the FCZM model. This can be inferred from the values β and α defined in Eqs. (25) and (26), respectively, as previously mentioned.

On the other hand, the behavior when shearing with initial compression is different and more complex. The peak stress goes beyond f_t when there is an initial compression σ_N, and keeps increasing whenever the initial compressive stress is increased. This can be observed in Figure 9(b), and in Figure 9(c) where higher compressive stresses are imposed. In addition, the residual stress is equal to $\mu\ \sigma_N$. One can see that for high compressive stresses like -20 MPa, the peak stress is equal to the residual stress, which is similar to the behavior captured when using Coulomb's interface model. This shows the transition from the Tvergaard's modified cohesive zone model to a frictional model like Coulomb's interface model as the imposed compressive stress increases. Note that Figure 9(c) shows the effect of the fourth case of α introduced in Eq. (26), while Figure 9(b) shows the effect of both the third and fourth case. Clearly, those introduced cases are responsible for the stiffer shear response under compression, which does not exist in the initial Tvergaard's CZM model. The CZM tangential behavior with initial compression is the same as the pure shear behavior, since λ itself depends on the positive normal displacement only according to Eq.(A.2), and the tangential stress σ_s is calculated by Eqs. (A.8) or (A.11), depending on the case, which is in both equations only affected by λ.

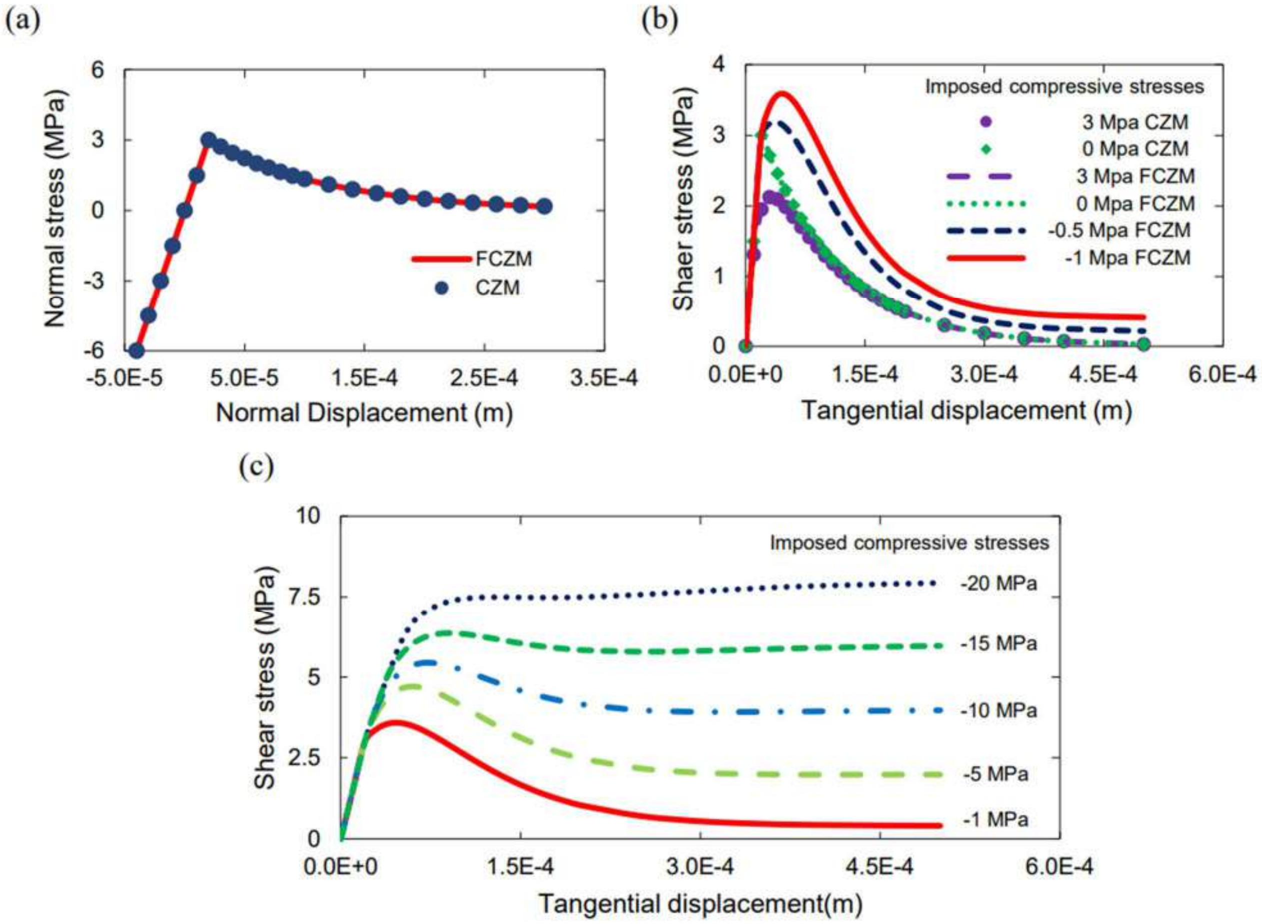

Figure 9. Simulations performed on one-interface element: (a) Normal stress versus the normal displacement for FCZM and CZM. Shear stress versus tangential displacement for the (b) FCZM and CZM under different imposed normal stresses, and for the (c) FCZM under higher imposed compressive stresses

Figure 10 (a) shows the two terms that form the total shear stress. As discussed before, one can see that the shear stress of the undamaged part of the interface behaves like a cohesive zone model, while the one of the damaged part behaves like a frictional model, with a nonlinear initial increase unlike Coulomb's interface model behavior.

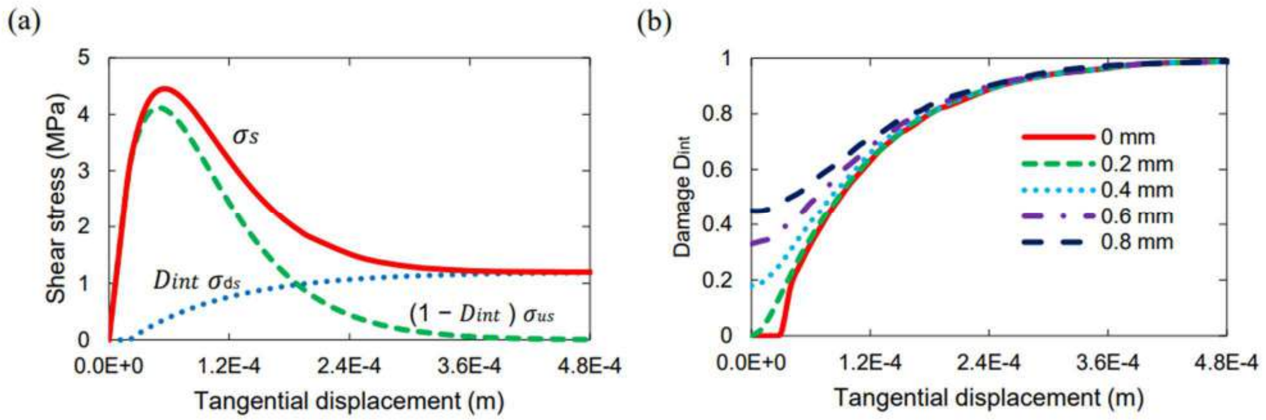

Figure 10. Simulations performed on one-interface element: (a) Total shear stress σ_s, damaged part's shear stress σ_{ds} multiplied by interface damage D_{int} and undamaged part's shear stress σ_{us} multiplied by $1 - D_{int}$, versus tangential displacement for the FCZM under -3 MPa initially imposed compressive stress. (b) Interface damage evolution for the FCZM under different initial normally imposed tensile displacements

The damage evolutions of the interface element under different initial normal imposed displacements are shown in Figure 10 (b). Since damage does not evolve under pure compression, its evolution under initial compression is the same as the evolution in the case without any initial imposed displacement. One can see that evolution is non-linear, due to the exponential evolution used in Tvergaard's model. The initial value of damage is related to the state of the interface before the application of the shear loading.

3.3 Calibration of the model using smooth bar

We describe in this section the main aspects related to the identification procedure of parameters of the FCZM, based on pull out test simulation results with smooth bar. From this calibration, simulations will be performed on tests with ribbed bar in the next section.

A group of simulations is performed using the newly implemented frictional cohesive zone model. Steel and concrete are assigned the models described in section 2.2 using the same methodology for the values of the damage parameters. Concrete's Young's modulus is considered 25 GPa, while concrete's ultimate tensile stress $f_{t\,con}$= 2.5 MPa, and concrete's fracture energy is 120 N/m. For the interface model, the parameters are initially varied in order to study their effect. The aim is to relate as much as possible each parameter to the materials properties, especially concrete, since the interface is the zone of contact between concrete and steel bar. The numerical mean bond stresses versus the free end displacements are compared to the experimental results extracted from [67].

Table 3. Final values assigned to the parameters of the FCZM in the simulations using the smooth bar and ribbed bar models

Parameter	$\boldsymbol{\delta_s}$	$\boldsymbol{f_t\ (MPa)}$	$\boldsymbol{G_f\ (N/m)}$	$\boldsymbol{\lambda_0 (m)}$	$\boldsymbol{\mu}$
Smooth bar	0.3	1.8	85	5e-5	0.3
Ribbed bar R1	0.16	2.16	97	5e-5	0.3
Ribbed bar R2	0.02	2.52	108	5e-5	0.3

As mentioned, in this procedure parameters are varied separately and in parallel, in order to study their effect on the general behavior. Four parameters are considered: f_t, λ_0, δ_s and G_f. After varying the parameters in parallel and analyzing different combinations, it has been observed that the parameters can be divided into two main categories, those that control principally the peak of the mean bond stress and it's maximum value: f_t, λ_0 and δ_s, while G_f controls the post peak behavior. In addition, a unique combination of the parameters f_t, λ_0 and δ_s gives a unique peak of mean bond stress and associated displacement. Thus, although it is possible to get a similar peak stress for two different values of f_t by changing both λ_0 and δ_s, the corresponding displacement at the peak is clearly not the same. Eventually, adjusting those four parameters will finally give a good fit. Those final values assigned to the parameters are shown in Table 3. The separate variation for each parameter is discussed below, in which a general calibration for each parameter is to be eventually concluded. In these separate variations, the other unvaried parameters are fixed to the values shown in Table 3.

Figure 11 (a) shows the results of the simulations for different values of f_t, all of which are considered to be less than or equal to $f_{t\,con}$. This is trivial since the interface layer is supposed to be a less stiff layer with many irregularities, thus it should not exceed the surrounding concrete in strength. One can see that f_t

obviously affects the peak stress. The value f_t= 1.8 MPa gives the best fit. Therefore, the ratio ξ between concrete tensile ultimate stress and the interface ultimate stress is ξ = 0.72. We assume that this identified ratio may be applied on the other simulations without any need to recalibration, according to the following formula:

$$f_t = \xi \, f_{t\,con} \tag{27}$$

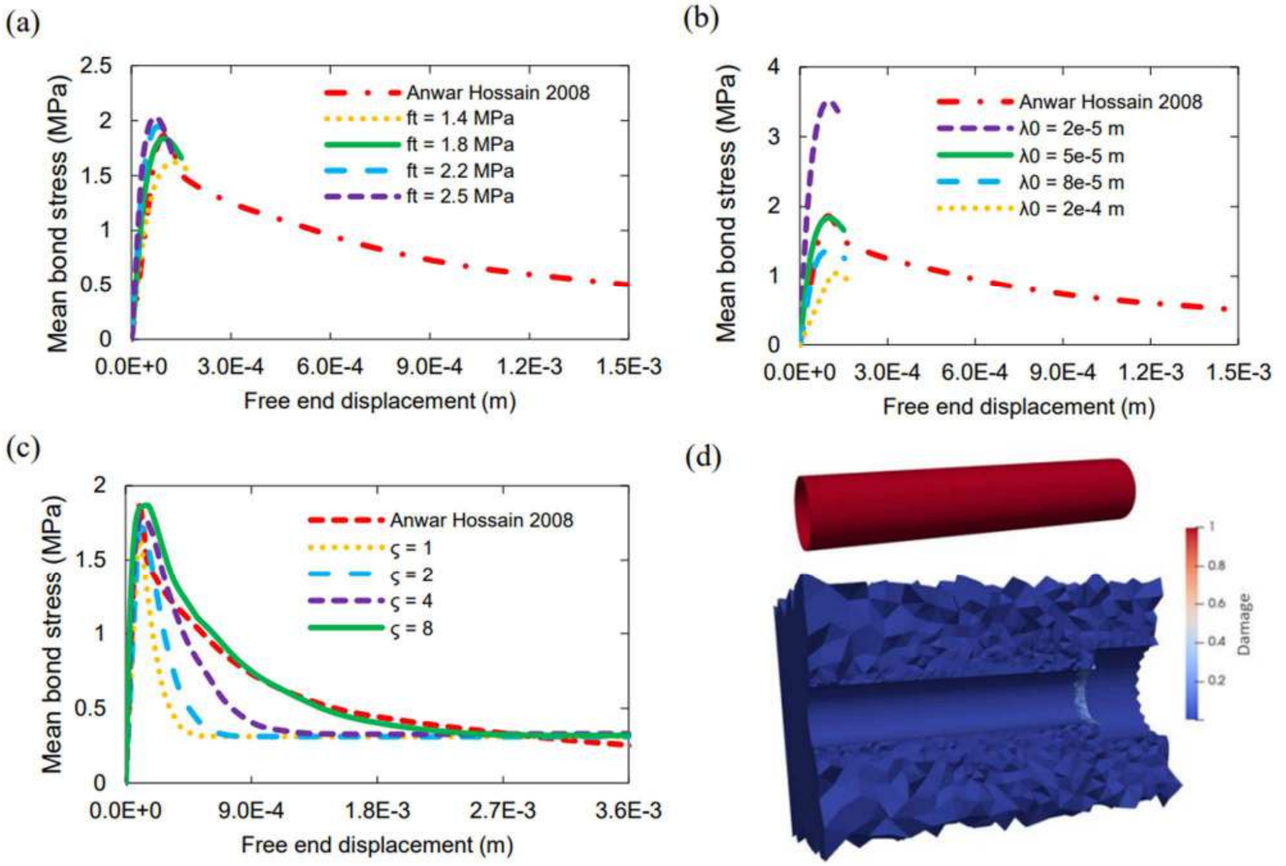

Figure 11. Simulations performed on the sample having a smooth bar. Plotting the mean bond stress versus free end displacement for the experimental data extracted from [67] and for the numerical results by varying: (a) f_t , (b) λ_0 and (c) ς. (d) Distribution of damage in the concrete and the interface for the reference simulation shown in green in (a), (b) and (c).

For the initial damage threshold λ_0, one can expect this value to be constant, just like concrete's initial damage strain parameter ε_{D_0} assigned in Mazars model in 2.3. This interface damage threshold λ_0 controls the displacement position of the peak stress and is identified as shown in Figure 11 (b). One can see that the best fit is obtained when λ_0= *5e-5 m* which will be used for the further simulations. Note that although this value affects both damage initiation in tension and in shearing, the shearing obviously dominates in such cases, which may explain this relatively high value of damage threshold.

In a similar way, the stiffness ratio δ_s is varied in order to get the best fit, which is reached when $\delta_s = 0.3$. This certainly sensitive ratio will be discussed in more details in the ribbed bar section. A formulation will be reached based on the smooth and the ribbed bar simulations, allowing us to identify the ratio without the need of predication from then on.

The fracture energy G_f of the interface is considered less than that of concrete, by using the same coefficient ξ previously identified, as follows:

$$G_f = \xi G_{f\,con} \tag{28}$$

In addition, the effect of the coefficient ς in Eq. (22) can be observed in Figure 11 (c). One can see that the best fit is when $\varsigma = 8$, which is considered the reference simulation. For other values of this coefficient ς, the post peak behavior is not very well reproduced. In particular, a more brittle post peak behavior is obtained for smaller values of ς. This coefficient will be kept constant in all simulations.

Finally, friction coefficient of the steel-concrete interface is considered 0.3, based on [73,74].

Thus, almost all the parameters are now related to the surrounding material, as shown in Table 4. The identified ratios and coefficients will be applied directly to the parameters in the ribbed bar simulations in order to check and verify the functionality of both of the calibration procedure and the FCZM.

Table 4. Values assigned to the parameters and the coefficients of the FCZM in the different simulations

<table>
<tr><th>Case</th><th>δ_s</th><th>$f_t\ (MPa)$</th><th>$G_f\ (N/m)$</th><th>$\lambda_0 (m)$</th><th>μ</th></tr>
<tr><td>Smooth</td><td>0.3</td><td rowspan="3">$\xi f_{t\,con}$</td><td rowspan="3">$\xi G_{f\,con}$</td><td rowspan="3">5e-5</td><td rowspan="3">0.3 based on [73,74]</td></tr>
<tr><td>R1</td><td>0.16</td></tr>
<tr><td>R2</td><td>$-0.3889\ \xi\ f_{t\,con} + 1$</td></tr>
<tr><td rowspan="3">All cases</td><td colspan="5">Coefficients</td></tr>
<tr><td colspan="2">ξ</td><td colspan="3">ς</td></tr>
<tr><td colspan="2">0.72</td><td colspan="3">8</td></tr>
<tr><td colspan="6">$f_{t\,con}$ in MPa ; $G_{f\,con}$ in N/m</td></tr>
</table>

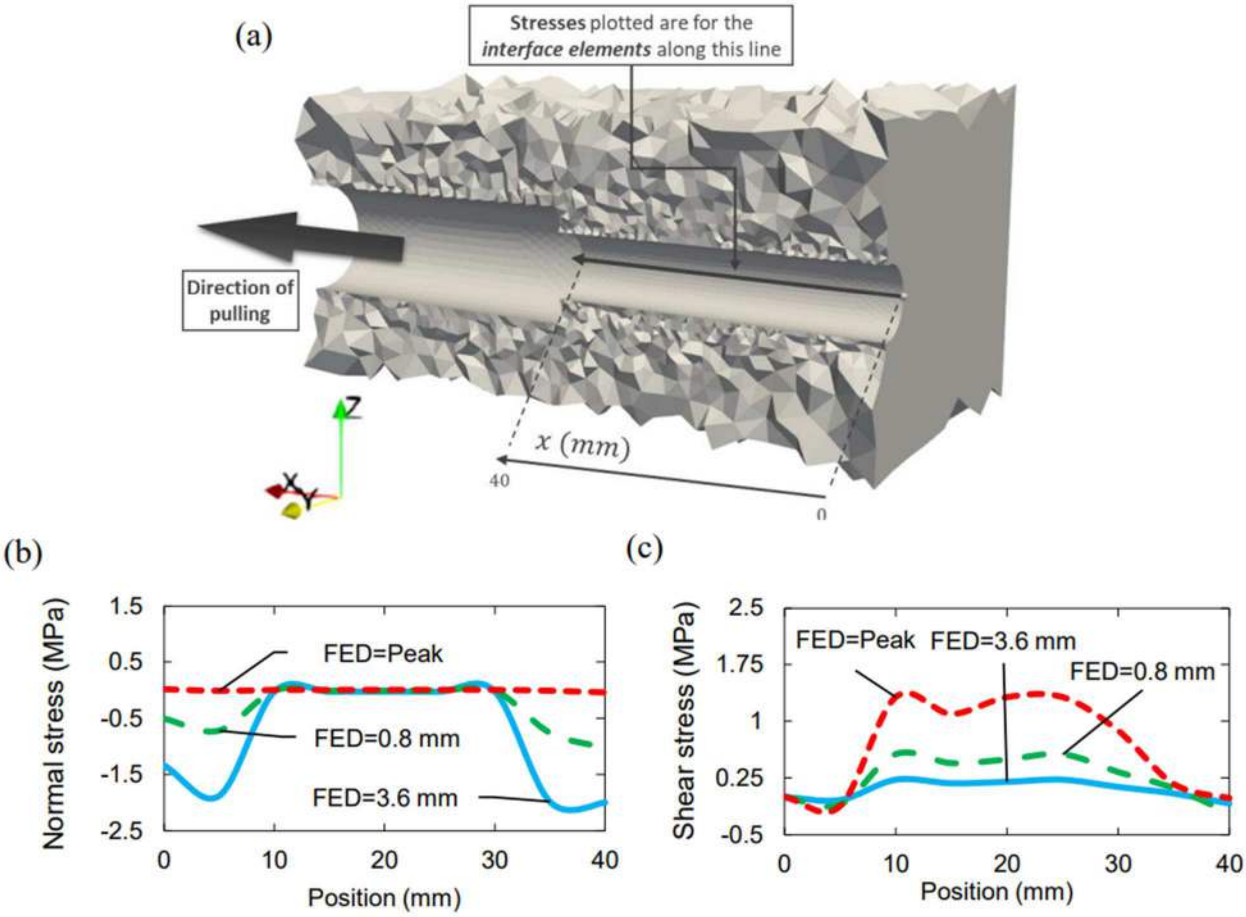

Figure 12. The reference simulation performed on the smooth sample. (a) A section at the central part of the concrete volume, showing a line at the steel-concrete interface considered for plotting, at three different free end displacements FED, the (b) normal stress and (c) shear stress S1 in the direction parallel to the axis of the steel bar.

The reference case simulation for the smooth bar, with the corresponding values for the parameters shown in Table 3 and Table 4, is considered. In Figure 11 (d), one can see that there is almost no visible damage in the concrete, but only in the fully damaged interface. This can explain the similarity between the interface model in shearing under compression and the result of the simulation, since the whole damage phenomena are mainly occurring at the interface itself. This eventually leads to the total loss of adhesion and the slipping of the steel bar without affecting significantly the concrete volume, but almost exclusively the steel-concrete interface. In Figure 12 one can observe the variation of normal and shear stresses of the interface elements as a function of the FED. Apparently, the normal compressive stress keeps increasing in magnitude after the post peak near the two ends of the interface, and those normal stresses are almost the same along the length of the interface in the central part at different moments during the simulation. Additionally, at the peak, the values near the ends of the interface are already very small and the normal stresses appears to be homogenous. On the other hand, the shear stresses are almost null near the ends of the interface while they are homogenous in the central part of the interface. The shear stresses decreases as the free end displacement keeps increasing. Such behavior is expected since the steel bar starts losing part of its adhesion.

One can expect this model to be applicable for different diameters of the smooth steel bars and for different sizes of the specimen. For instance, by modeling a bigger sample, having a 10 mm diameter bar, and 125 mm side length of the cubic concrete sample, and using the same properties of the aforementioned reference simulation for all the materials including the FCZM, the same macroscopic behavior can be observed as shown in Figure 13. Note that the quantity of interest here is the mean bond stress which implicitly includes the effect of the bar diameter, see Eq. (14). Due to its cylindrical geometry, the smooth bar response is mainly affected by the interface model, and barely affected by the surrounding concrete, which explains the behavior observed.

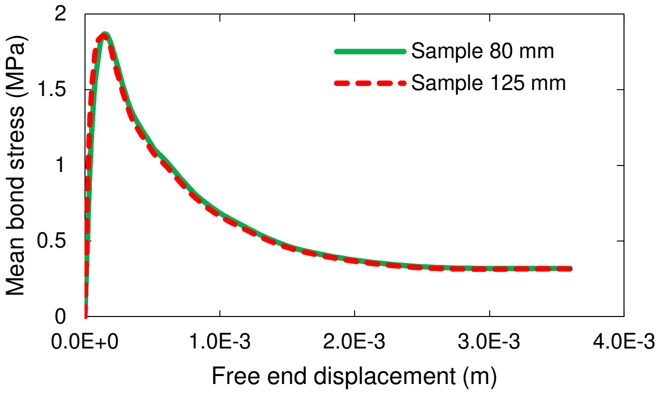

Figure 13 Mean bond stress versus free end displacement for the numerical simulations performed on the two samples having a smooth bar. Sample 80 mm: diameter of the bar is 8 mm, adhesive length is 40 mm and side length of the concrete cube is 80 mm. Sample 125 mm: diameter of the bar is 10 mm, adhesive length is 125 mm and the side length of concrete cube is 125 mm

3.4 Application on a pull out test with ribbed bar

Following the verification of the ability of the FCZM to capture the behavior of the pull-out test on a sample with a smooth bar, we now assess in this section its performance on a more complex and common case with a spiral-ribbed bar. Pull-out test simulations are then performed with ribbed bars, to complete and verify the calibration process of the FCZM in such cases. Two samples are used having different diameter of steel bar, and the corresponding pull-out test results are compared to experimental data extracted from [30,75]. Numerical results are finally analyzed more deeply in terms of local stresses and damage.

3.4.1 Sample

A new sample is modelled using the same procedure with a steel bar with spiral ribs. The diameter d of the bar is taken equal to 8 mm, and the cubic sample length is 80 mm, which is in accordance with the recommended pull-out test (10d height). In addition, the steel bar embedded length is also 80 mm, divided equally into adhesive and non-adhesive lengths. The dimensions of the steel bar are detailed in Figure 14. The steel bar modelled, which is based on the standard shape and dimensions of a spiral-ribbed bar, can be described as follows:

- Core: it has a cylindrical shape, whose radius is the radius of the steel bar. Its length is the total embedded length of the steel bar in the concrete sample in a pull-out (adhesive and non-adhesive length).
- Longitudinal ribs: the bar has two longitudinal ribs along the length of the cylinder that are exactly opposite to each other, having an isosceles trapezoidal section.
- Transversal ribs: Each rib spans from one of the longitudinal ribs to the other longitudinal rib, thus covering half a circle (an angle of 180°) and it is inclined a certain angle with respect to the plane whose normal vector is the axis of the bar. In addition, the ribs on one side are symmetric to the ribs of the other side with respect to the axis of the steel bar.

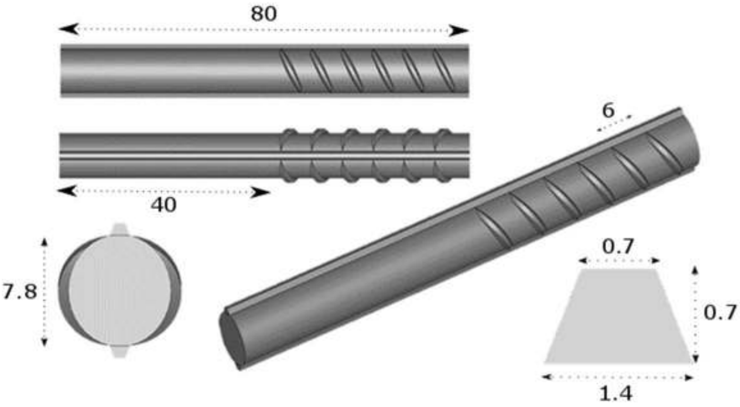

Figure 14. Detailed dimensions of the modeled spiral-ribbed steel bar (in mm)

Similarly to the smooth bar case, both geometry and meshing are generated with the Salome platform. The number of meshing elements in the concrete is 308 000 elements, whose triangular edge size at the interface is equal to 0.4 mm while at the external surface of concrete the size is almost 5 mm. In addition, the average size of elements in the steel bar is 0.4 mm resulting in about 298 000 elements.

3.4.2 Complementary calibration process

Two simulations, named R1 and R2, are performed using the ribbed samples. The pull-out test experimental results used in the first simulation R1 for comparison are those derived from [75]. The diameter of the ribbed bar is 8 mm, and the length of the steel bar is 80 mm, as indicated in Figure 14, and so is the cubic concrete sample side length.

In first simulation R1, steel and concrete are assigned the models described in section 2.2 using the same methodology for the values for the damage parameters. In addition, based on the experimental data, concrete's Young's modulus is considered 30 GPa, while concrete's ultimate tensile stress $f_{t\,con}$= 3 MPa. The corresponding fracture energy is 130 N/m. Also for the FCZM, the values assigned to the parameters are shown in Table 3 and Table 4.

The initial value extracted from the smooth bar simulation for δ_s cannot actually produce the experimental behavior. Thus, the stiffness ratio δ_s is assigned a different value in each simulation in order to understand its effect on the overall behavior, and in order to complete the calibration process before final validation. The mean bond stresses versus displacements along with the experimental results extracted from [75] are shown in Figure 15.

By considering the case produced when $\delta_s = 0.16$, one can see that the macroscopic curve agrees in general with experimental results, but when the value of δ_s is lower, the behavior seems to be much stiffer at later stages, and it is much weaker when this value is greater than or equal to unity. Still, at the beginning of the loading phase, one can see an initial change of slope for all four cases. This transition of slope is smooth when δ_s is smaller, while it tends to form an initial peak when this value is higher. Obviously, one needs to assign a value for δ_s smaller than 1 in order to capture a more realistic behavior.

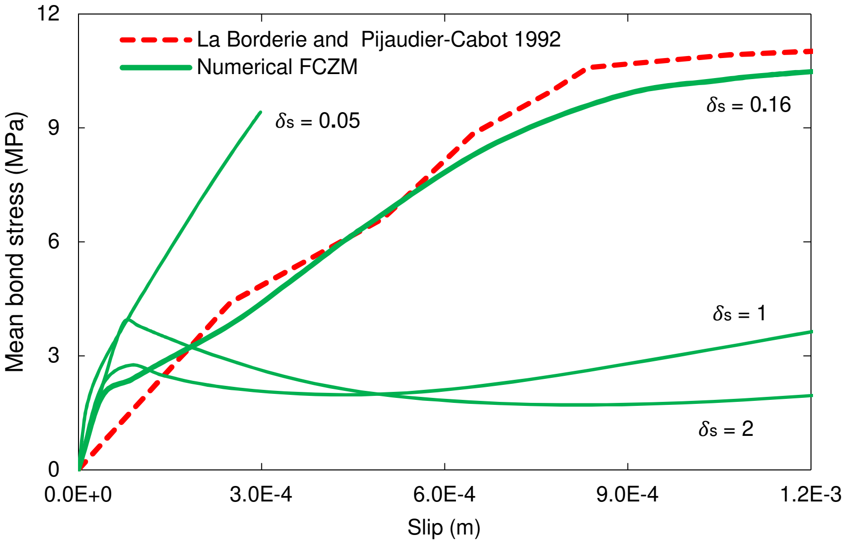

Figure 15. Mean bond stress versus slip for the numerical simulations R1 performed using different stiffness ratios δ_s on the sample having a ribbed bar and the corresponding experimental results extracted from [75]

One can see that the two stiffness ratios used for the smooth bar simulation and the ribbed bar R1 simulation are different. A certain relation should be proposed in order to prevent the predication of this parameter in each simulation. Since K_n depends uniquely on f_t and λ_0 according to Eq.(A.7), and since δ_s is a direct ratio between K_n and K_s according to Eq. (A.3), one can relate δ_s to both parameters. However, by taking into consideration that λ_0 was kept constant in both cases, and by taking into account the variation of the ultimate tensile stress f_t of the interface in each case, one can propose a direct linear interpolation between δ_s and f_t. For instance, by considering the smooth bar simulation values, which are f_t = 1.8 MPa and δ_s = 0.3, and the ribbed bar R1 simulation values, which are f_t = 2.16 MPa and δ_s = 0.16, the following linear formulation is proposed:

$$\delta_s = -0.3889 \times 10^{-6}\, f_t + 1$$

$$\delta_s = -0.3889 \times 10^{-6}\ \xi\, f_{t\,con} + 1 \qquad \textbf{(29)}$$

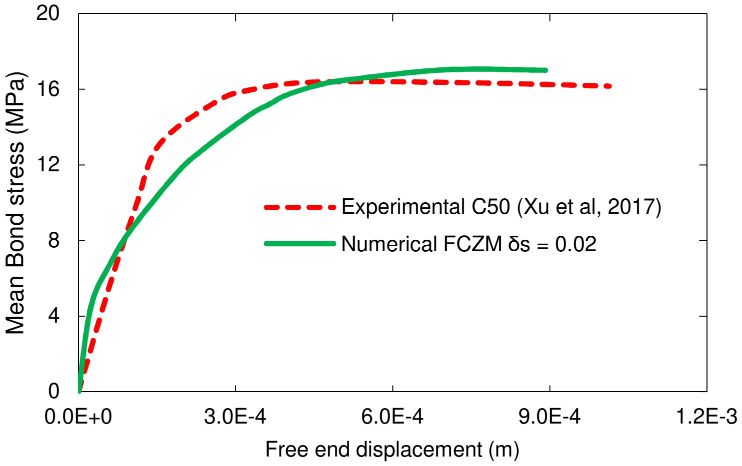

Figure 16. Mean bond stress versus free end displacement for the numerical simulation R2 performed on the sample having a ribbed bar and the corresponding experimental results extracted from [30]

In order to verify the applicability of this relation and more generally of the whole calibration procedure, another simulation on a ribbed bar sample is performed. The pull-out test experimental results used in this second simulation termed R2 for comparison are those derived from [30]. The test results considered are those of specimen M-C50-F0, which includes high strength concrete C50 with a ribbed steel bar. The diameter of the bar is 16 mm, while its adhesive length is 80 mm. Hence, a new sample is generated based on the properties of the experimental sample.

Similarly to what was previously done, steel and concrete are assigned the models described in section 2.2 using the same methodology for the values for the damage parameters of concrete. In addition, according to the properties of the sample, concrete's Young's modulus is considered 35 GPa, while concrete's ultimate tensile stress $f_{t\ con}$= 3.5 MPa. The corresponding fracture energy is 150 N/m. Also for the FCZM, the values assigned to the parameters are shown in Table 3 and Table 4. The corresponding results are shown in Figure 16 .

One can see that the general behavior is correctly reproduced using the assigned values for the FCZM parameters. Thus, the FCZM is able to reproduce ribbed bar pullout test behaviors by applying simple formulations for the parameters, by assigning to the FCZM parameters the values shown in Table 4.

3.4.3 Discussions on the ribbed samples results

The FCZM was able to correctly reproduce the macroscopic stress-slip behavior using ribbed bars. One question could arise about the importance of the FCZM friction in the ribbed bar when compared to the smooth bar. Unlike the smooth bar, whose bond is governed by friction due to the absence of ribs, the interaction phenomena in the ribbed bar are controlled by both friction and mechanical interlock. When ignoring the geometry of the ribs at the macroscopic scale, this coefficient cannot be considered the same, since the geometrical interlock should be included to differentiate between a smooth and a ribbed bar. The macroscopic friction in this case may be seen as a combination of the effects of the usual steel-concrete friction and mechanical interlock. On the other hand, using the same friction coefficient at the mesoscopic scale could be justified by the fact that this coefficient is supposed to reflect exactly the friction between steel and concrete, excluding the geometrical interlock which is explicitly accounted for. To investigate this aspect, another simulation is performed using the same parameters of simulation R1, but changing the friction coefficient μ from 0.3 to 0.001 (almost zero). The mean bond stress versus free end displacement results are compared in Figure 17. One can see that the frictional part of the model plays an important role in the behavior, and it increases with the increase of the displacement, which is excepted since the bar starts losing adhesion. This result shows that it is realistic to take the same friction coefficient, as along as the effect of the mechanical interlock is reproduced separately. In a future study, the effect of the rib shape (angle, width, height, orientation) on the bond behavior will be investigated in details.

The model use fine mesh to reach accurate results in terms of macroscopic behavior, and for visualizing stresses and damage in concrete locally. To understand the importance of the meshing, the sample used in the R1 simulation is re-meshed using relatively a very coarse mesh. For the new coarse sample, the number of mesh elements in the concrete is 42 000 while it is 22 000 in the steel bar. A simulation is performed using the same values for the parameters as the R1 simulation, and the mean bond stress versus free end displacement responses are compared in Figure 17. One can see that the sample with coarse mesh shows a different macroscopic behavior. The effect is up to 40% at the end of the simulation, and cannot be neglected. This justifies the need to use finer meshes at this scale to prevent such dependency on the mesh.

It should be noted that even finer meshes could be used, and we have verified on one example that the corresponding results (not shown here for conciseness) are close to the one shown in Fig. 17 with a much higher computational cost and harder convergence. We then consider that the mesh size retained is an acceptable compromise between accuracy and computational difficulties. For instance, the most important region to be meshed is the internal concrete region surrounding the steel-concrete interface, which has a direct effect on the interface behavior where the FCZM is applied. Furthermore, it is important to have a fine mesh at the interface, in order to correctly reproduce the geometry of the ribs and their effect, as previously discussed, as any change in the geometry of the ribs affects the bond strength.

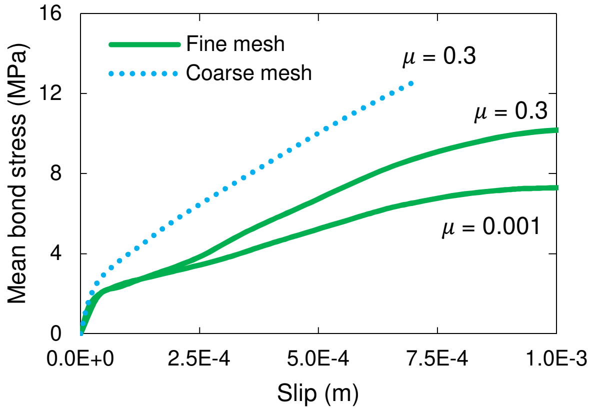

Figure 17 Mean bond stress versus free end displacement for the numerical simulations performed on the sample having a ribbed bar: simulation R1 with fine mesh and friction coefficient μ=0.3; simulation (2) with fine mesh and μ=0.001; simulation (3) with very coarse mesh and μ=0.3

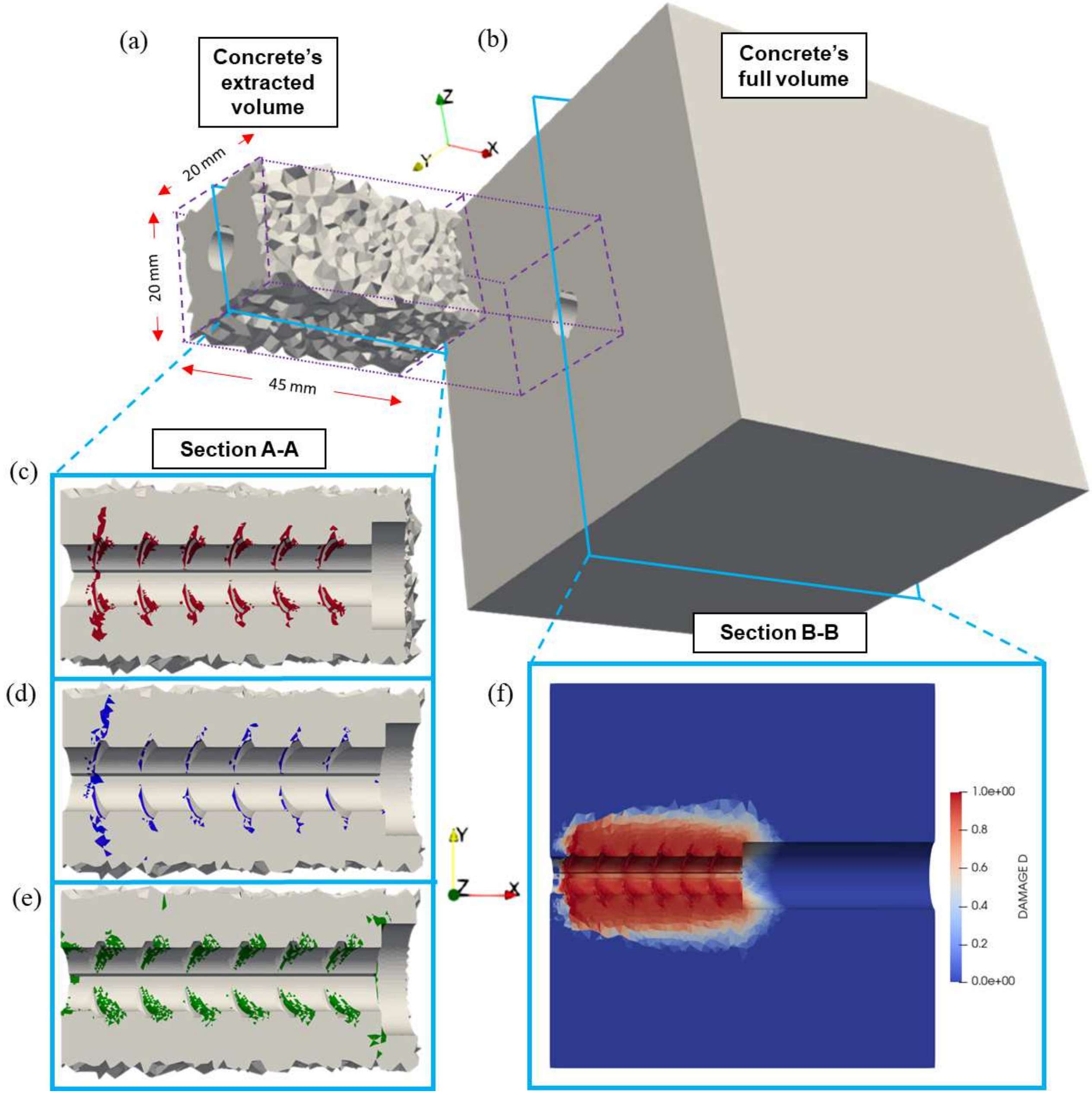

Figure 18. Visualization of the concrete part of the spiral sample used in simulation R1. Concrete's (a) extracted volume and (b) full volume. Section A-A is at the central part of the extracted volume showing: (c) Full cracks (in red) representing the regions where D>0.99, (d) concrete regions (in blue) having tensile principle stresses in the three principle directions and (e) concrete regions (in green) having compressive principle stresses in the three principle directions. (f) Section B-B that is at the central part of the concrete volume, which shows the distribution of damage *D* in the concrete

Distribution of damage and principle stresses for the simulation R1 are shown in Figure 18. By observing distribution of the damage D in the concrete shown in Figure 18(c) for the simulation R1, one can see that the fully damaged cracks are similar to what was observed in other studies like [25]. It can be described by a crack at each rib and an inclined crack at the last rib. One can observe that concrete is fully damaged at the ribs, and less damaged in between two ribs. On the other hand, the interface is fully damaged everywhere. Such damaged concrete is what is expected at the surface of contact, and what is observed experimentally. It is because the ribs prevent the bar from slipping, thus applying an additional pressure on the surrounding concrete, which leads to the initiation of the inclined cracks at the top of each rib. However, the damage inside the concrete has clearly propagated quickly. In Figure 18(d), one can see that the elements having tensile principle stresses in all three directions are at the top of the ribs and a certain extension behind the last rib. This coincides with the fully damage pattern observed in Figure 18(c). On the other hand, Figure 18(e) shows that the concrete elements in front of the ribs have compressive stresses in the three principle directions. This can be related to the phenomena of crashing that occurs at this area because of the movement of the ribs when applying the pulling effort. In Figure 19, we can observe the existence of very large compressive stresses in some of the elements. These entire elements are in front of the ribs. Thus, they are all subjected to compressive stresses in the three principal directions. The behavior is very complex near steel-concrete interface and it is difficult to extract any experimental results from pull-out tests at this scale. Due to the lack of any experimental data that quantify or visualize this phenomenon, one cannot evaluate and compare the principle stresses obtained, in order to verify these results. The existence of such very high compressive stresses can be related to the concrete's model. Hence, in the near future, it could be instructive to investigate more deeply the behavior in this region with different approaches to model the concrete behavior in compression.

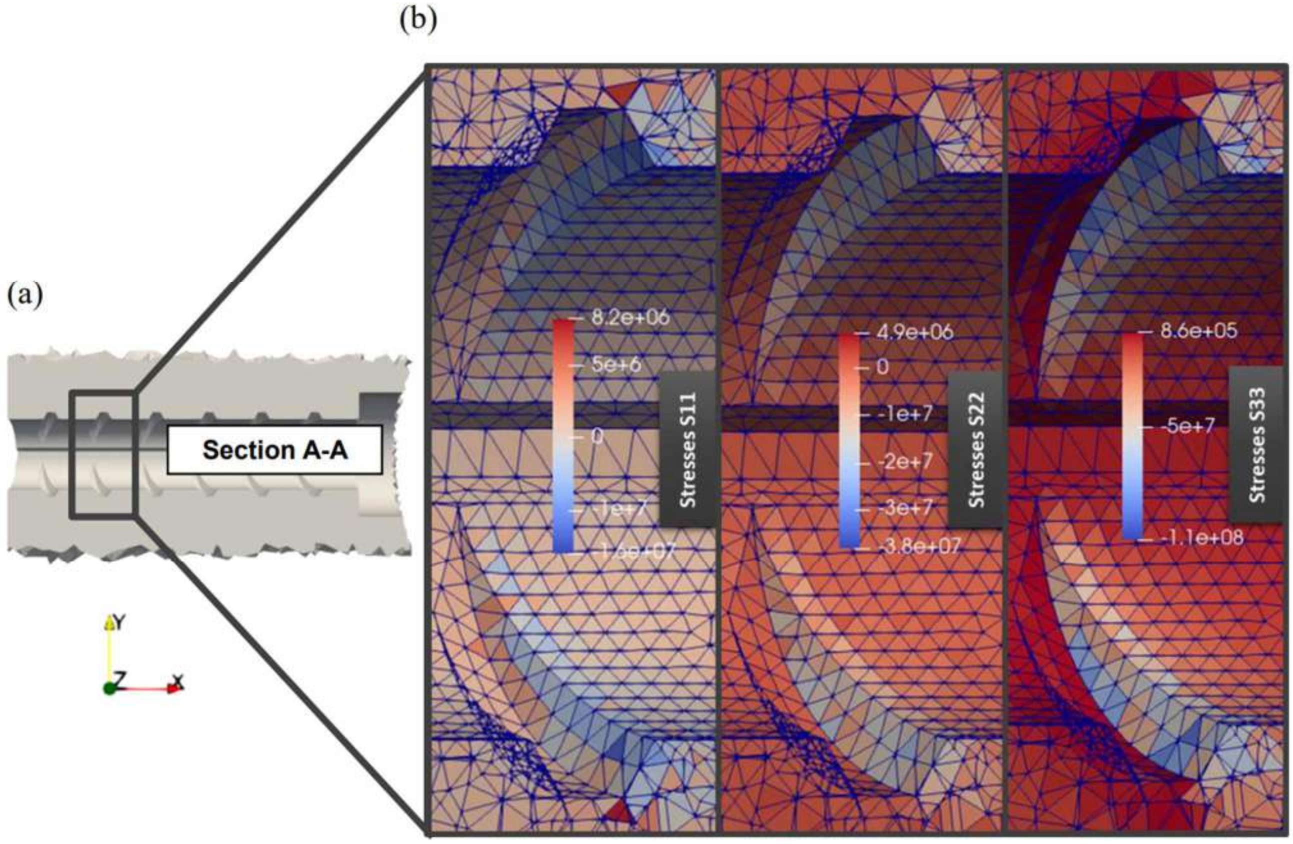

Figure 19 A closer look at the scale of the rib of the spiral sample used in simulation R1. (a) Section A-A previously extracted in Figure 18; (b) Distribution of the three principle stresses in a specific region at the steel-concrete surface of contact.

The FCZM was developed to help study the behavior of steel-concrete bond at the mesoscopic scale, through the mean bond stress-displacement behavior and distributions of the damage and stresses. It can be used to investigate the effects of many phenomena and aspects that are hardly observed when using macroscopic models. For instance, the FCZM could be used in a mesoscopic study to elaborate the effect of including coarse aggregates in the concrete mix, instead of homogenous concrete as considered in here. As mentioned above, it can also help in understanding the effect of the geometry of the ribs on the bond behavior. These geometries are usually ignored on a macroscopic scale, which is used to model bigger structures. Thus, it may aid in giving additional information about the parameters that should be included in the macroscopic models, and/or in calibrating these parameters. Still, this model is not only specific to the steel-concrete interface. It can be applied for other engineering applications like assigning it to the mortar joint of the masonry walls [76], UHPC-NC composite member [77], timber-concrete interface [49] and many other composite-like materials in which CZM is applied, but where the frictional effect could be important like fiber-matrix interfaces [39,40] and aggregates-mortar interface [19].

4 CONCLUSION AND PERSPECTIVES

In this paper, a 3D mesoscopic approach is applied to study the behavior at the steel concrete interface. Due to the importance of the interfacial model between steel and concrete, different models were used to represent this surface. A newly implemented interface model was presented in this paper in order to simulate this phase, due to the inability of both the modified Tvergaard's cohesive zone model and the frictional Coulomb's interface model to simulate the behavior of a pull out test with smooth bar. This newly implemented frictional cohesive zone model (FCZM) is a combination of the two aforementioned interface models. Further, the Mazars damage model is used in the concrete to represent the fracture phenomena, i.e. initiation and propagation of cracks. It is supplemented by a Hillerborg regularization in tension and modifications applied in compression in order to prevent a mesh dependency of the damaged response in compression.

The results have shown good agreement with experimental data in pull out samples having a smooth bar and a spiral-ribbed bar. For the ribbed bar, the experimental behavior was reproduced eventually with parameters calibrated on the smooth bar case by applying simple formulations that relate the volumetric materials properties to the FCZM parameters, with no need for further adjustments. It has been observed that the geometry of the bar plays a significant role in the overall behavior, and so does friction even in ribbed bar, showing the importance of coupling these two aspects. This paves the way for studying the effects of different shapes of the ribs, in terms of height, thickness, angle and overall orientation, on the bond stress at the mesoscopic scale. In addition, coarser mesh produces importantly different stress-slip bond results, which forces the usage of fine meshes and leads to higher computational cost. The full damage pattern was very similar to what can be observed in previous numerical simulations in literature, by observing one crack at the top of each rib and an extended crack at the last rib. In addition, the general damage distribution has shown a fast propagation. Moreover, it has been shown that the regions with fully damaged concrete are mostly under tensile stresses or compressive stresses in the three principal directions. On the other hand, the regions in front of the ribs are all under compressive stresses in three directions, at which very high compressive stresses were observed.

In the future, a more accurate analysis of the distribution of damage and stresses in the concrete near the interfaces will be carried out with a different model for concrete behavior; in particular, the effects of tri-compressive states of stresses will be investigated by means of consistent and appropriate criteria. One possibility is to propose a phase field approach by taking different criterions in tension and compression. In addition, the effect of creep and shrinkage of concrete on the overall behavior is to be analyzed with the influence of the loading and environmental conditions, as well as the impact of material properties changes due to the use of different types of cement. Furthermore, as mentioned above an important point that will be studied is the influence of different shapes of the ribs of the steel bar on the simulation. Finally, a more accurate analysis of the effects of the aggregate packing around the steel bar on the damage development would deserve to be studied, using different shapes and sizes of aggregates and various dimensions of concrete covers.

REFERENCES

[1] A. Casanova, L. Jason, L. Davenne, Bond slip model for the simulation of reinforced concrete structures, Engineering Structures. 39 (2012) 66–78. https://doi.org/10.1016/j.engstruct.2012.02.007.

[2] C. Andrade, C. Alonso, F. Molina, Cover cracking as a function of rebar corrosion: Part II–Numerical model, Materials and Structures. 26 (1993) 532–548. https://doi.org/doi.org/10.1007/BF02472864.

[3] K. Bhargava, A.K. Ghosh, Y. Mori, S. Ramanujam, Model for cover cracking due to rebar corrosion in RC structures, Engineering Structures. (2006) 17. https://doi.org/10.1016/j.engstruct.2005.11.014.

[4] Q.T. Nguyen, S. Caré, Y. Berthaud, A. Millard, F. Ragueneau, Experimental and numerical behaviour of reinforced mortar plates subjected to accelerated corrosion, International Journal for Numerical and Analytical Methods in Geomechanics. 35 (2011) 1141–1159. https://doi.org/10.1002/nag.947.

[5] T.T.H. Nguyen, B. Bary, T. de Larrard, Coupled carbonation-rust formation-damage modeling and simulation of steel corrosion in 3D mesoscale reinforced concrete, Cement and Concrete Research. 74 (2015) 95–107. https://doi.org/10.1016/j.cemconres.2015.04.008.

[6] K. Suda, S. Misra, K. Motohashi, Corrosion products of reinforcing bars embedded in concrete, Corrosion Science. 35 (1993) 1543–1549. https://doi.org/10.1016/0010-938X(93)90382-Q.

[7] M. Liu, L. Jin, R. Zhang, F. Chen, X. Du, Combined effect of corrosion and strain rate on the bond behavior: A two-stage simulation, International Journal of Mechanical Sciences. 227 (2022) 107438. https://doi.org/10.1016/j.ijmecsci.2022.107438.

[8] M. Liu, L. Jin, F. Chen, R. Zhang, X. Du, 3D meso-scale modelling of the bonding failure between corroded ribbed steel bar and concrete, Engineering Structures. 256 (2022) 113939. https://doi.org/10.1016/j.engstruct.2022.113939.

[9] A. Ibrahimbegovic, A. Boulkertous, L. Davenne, D. Brancherie, Modelling of reinforced-concrete structures providing crack-spacing based on X-FEM, ED-FEM and novel operator split solution procedure: MODELLING OF RC STRUCTURES, Int. J. Numer. Meth. Engng. 83 (2010) 452–481. https://doi.org/10.1002/nme.2838.

[10] L.N. Lowes, J.P. Moehle, S. Govindjee, Concrete-Steel Bond Model for Use in Finite Element Modeling of Reinforced Concrete Structures, ACI Structural Journal. (2004) 12.

[11] G. Monti, F.C. Filippou, E. Spacone, Analysis of hysteretic behavior of anchored reinforcing bars, Structural Journal. 94 (1997) 248–261.

[12] D. Ngo, A.C. Scordelis, Finite Element Analysis of Reinforced Concrete Beams, ACI Journal Proceedings. 64 (1967) 152–163. https://doi.org/10.14359/7551.

[13] B. Richard, F. Ragueneau, C. Cremona, L. Adelaide, J.L. Tailhan, A three-dimensional steel/concrete interface model including corrosion effects, Engineering Fracture Mechanics. 77 (2010) 951–973. https://doi.org/10.1016/j.engfracmech.2010.01.017.

[14] A. Caballero, C.M. López, I. Carol, 3D meso-structural analysis of concrete specimens under uniaxial tension, Computer Methods in Applied Mechanics and Engineering. 195 (2006) 7182–7195. https://doi.org/10.1016/j.cma.2005.05.052.

[15] A. Daoud, O. Maurel, C. Laborderie, 2D mesoscopic modelling of bar–concrete bond, Engineering Structures. (2013) 12. https://doi.org/10.1016/j.engstruct.2012.11.018.

[16] D. Nguyen, C. Lawrence, C. La Borderie, M. Matallah, G. Nahas, A mesoscopic model for a better understanding of the transition from diffuse damage to localized damage, European Journal of Environmental and Civil Engineering. 14 (2010) 751–776.

[17] V.P. Nguyen, M. Stroeven, L.J. Sluys, Multiscale failure modeling of concrete: Micromechanical modeling, discontinuous homogenization and parallel computations, Computer Methods in Applied Mechanics and Engineering. 201–204 (2012) 139–156. https://doi.org/10.1016/j.cma.2011.09.014.

[18] Y. Wang, Y. Zheng, X. Wang, Mesoscopic damage evolution on bonding interface and its influence on macroscopic performance deterioration of reinforced concrete member, International Journal of Computational Materials Science and Engineering. 8 (2019) 1950005.

[19] T. Wu, P. Wriggers, Multiscale diffusion–thermal–mechanical cohesive zone model for concrete, Comput Mech. 55 (2015) 999–1016. https://doi.org/10.1007/s00466-015-1149-y.

[20] J. Zhang, Z. Wang, H. Yang, Z. Wang, X. Shu, 3D meso-scale modeling of reinforcement concrete with high volume fraction of randomly distributed aggregates, Construction and Building Materials. 164 (2018) 350–361.

[21] L. Eddy, K. Nagai, Numerical simulation of beam-column knee joints with mechanical anchorages by 3D rigid body spring model, Engineering Structures. 126 (2016) 547–558. https://doi.org/10.1016/j.engstruct.2016.07.054.

[22] D. Hayashi, K. Nagai, L. Eddy, Mesoscale Analysis of RC Anchorage Performance in Multidirectional Reinforcement Using a Three-Dimensional Discrete Model, J. Struct. Eng. 143 (2017) 04017059. https://doi.org/10.1061/(ASCE)ST.1943-541X.0001780.

[23] L. Jin, X. Li, R. Zhang, X. Du, Modelling of bond behavior of deformed bar embedded in concrete after heating to high temperatures: A mesoscale study, Construction and Building Materials. 334 (2022) 127456. https://doi.org/10.1016/j.conbuildmat.2022.127456.

[24] L. Jin, X. Li, R. Zhang, X. Du, Bond-slip behavior between concrete and deformed rebar at elevated temperature: Mesoscale simulation and formulation, International Journal of Mechanical Sciences. 205 (2021) 106622. https://doi.org/10.1016/j.ijmecsci.2021.106622.

[25] L. Jin, M. Liu, R. Zhang, X. Du, 3D meso-scale modelling of the interface behavior between ribbed steel bar and concrete, Engineering Fracture Mechanics. 239 (2020) 107291. https://doi.org/10.1016/j.engfracmech.2020.107291.

[26] Y. Yamamoto, H. Nakamura, I. Kuroda, N. Furuya, Simulation of crack propagation in rc shear wall using a 3d rigid-body-spring model with random geometry, European Journal of Enviromental and Civil Enginiring. 18 (2014) 780–792.

[27] Z.P. Bazant, M.R. Tabbara, M.T. Kazemi, G. Pijaudier-Cabot, Random Particle Model for Fracture of Aggregate or Fiber Composites, J. Eng. Mech. 116 (1990) 1686–1705. https://doi.org/10.1061/(ASCE)0733-9399(1990)116:8(1686).

[28] P. Grassl, A lattice approach to model flow in cracked concrete, Cement and Concrete Composites. 31 (2009) 454–460.

[29] H. Lin, Y. Zhao, P. Feng, H. Ye, J. Ozbolt, C. Jiang, J.-Q. Yang, State-of-the-art review on the bond properties of corroded reinforcing steel bar, Construction and Building Materials. 213 (2019) 216–233. https://doi.org/10.1016/j.conbuildmat.2019.04.077.

[30] S. Xu, A. Li, H. Wang, Bond properties for deformed steel bar in frost-damaged concrete under monotonic and reversed cyclic loading, Construction and Building Materials. 148 (2017) 344–358. https://doi.org/10.1016/j.conbuildmat.2017.05.090.

[31] F. Bernard, S. Kamali-Bernard, W. Prince, 3D multi-scale modelling of mechanical behaviour of sound and leached mortar, Cement and Concrete Research. (2008) 10.

[32] M. Raous, M.A. Karray, Model coupling friction and adhesion for steel- concrete interfaces, (2010) 10.

[33] R. Serpieri, G. Alfano, Bond-slip analysis via a thermodynamically consistent interface model combining interlocking, damage and friction, Int. J. Numer. Meth. Engng. 85 (2011) 164–186. https://doi.org/10.1002/nme.2961.

[34] G.I. Barenblatt, The Mathematical Theory of Equilibrium Cracks in Brittle Fracture, in: H.L. Dryden, T. von Kármán, G. Kuerti, F.H. van den Dungen, L. Howarth (Eds.), Elsevier, 1962: pp. 55–129. https://doi.org/10.1016/S0065-2156(08)70121-2.

[35] D.S. Dugdale, Yielding of steel sheets containing slits, Journal of the Mechanics and Physics of Solids. 8 (1960) 100–104. https://doi.org/10.1016/0022-5096(60)90013-2.

[36] S. Li, M. Thouless, A. Waas, J. Schroeder, P. Zavattieri, Use of a cohesive-zone model to analyze the fracture of a fiber-reinforced polymer-matrix composite, Composites Science and Technology. 65 (2005) 537–549. https://doi.org/10.1016/j.compscitech.2004.08.004.

[37] M. Elices, C. Rocco, C. Roselló, Cohesive crack modelling of a simple concrete: Experimental and numerical results, Engineering Fracture Mechanics. (2009) 13.

[38] A. Needleman, A continuum model for void nucleation by inclusion debonding, (1987).

[39] M. Heshmati, R. Haghani, M. Al-Emrani, A. André, On the strength prediction of adhesively bonded FRP-steel joints using cohesive zone modelling, Theoretical and Applied Fracture Mechanics. 93 (2018) 64–78. https://doi.org/10.1016/j.tafmec.2017.06.022.

[40] W. zhang, Y. Huang, Three-dimensional numerical investigation of mixed-mode debonding of FRP-concrete interface using a cohesive zone model, Construction and Building Materials. 350 (2022) 128818. https://doi.org/10.1016/j.conbuildmat.2022.128818.

[41] X. Xiong, Q. Xiao, Meso-scale simulation of bond behaviour between retarded-bonded tendons and concrete, Engineering Structures. 228 (2021) 111410. https://doi.org/10.1016/j.engstruct.2020.111410.

[42] G. Alfano, E. Sacco, Combining interface damage and friction in a cohesive-zone model, Int. J. Numer. Meth. Engng. 68 (2006) 542–582. https://doi.org/10.1002/nme.1728.

[43] R. Serpieri, G. Alfano, E. Sacco, A mixed-mode cohesive-zone model accounting for finite dilation and asperity degradation, International Journal of Solids and Structures. 67–68 (2015) 102–115. https://doi.org/10.1016/j.ijsolstr.2015.04.005.

[44] R. Serpieri, E. Sacco, G. Alfano, A thermodinamically consistent derivation of a frictional-damage cohesive-zone model with different mode I and mode II fracture energies, (2015) 30.

[45] M. Albarella, R. Serpieri, G. Alfano, E. Sacco, A 3D multiscale cohesive zone model for quasi-brittle materials accounting for friction, damage and, (2015) 28. https://doi.org/10.1080/17797179.2015.1096674.

[46] R. Serpieri, M. Albarella, G. Alfano, E. Sacco, Analysis of failure in quasi-brittle materials by 3D multiplane cohesive zone models combining damage, friction and interlocking, Procedia Structural Integrity. 3 (2017) 441–449. https://doi.org/10.1016/j.prostr.2017.04.066.

[47] R. Serpieri, M. Albarella, E. Sacco, A 3D two-scale multiplane cohesive-zone model for mixed-mode fracture with finite dilation, Computer Methods in Applied Mechanics and Engineering. 313 (2017) 857–888. https://doi.org/10.1016/j.cma.2016.10.021.

[48] G. Alfano, M.A. Crisfield, Finite element interface models for the delamination analysis of laminated composites: mechanical and computational issues, Int. J. Numer. Meth. Engng. 50 (2001) 1701–1736. https://doi.org/10.1002/nme.93.

[49] J. Jaaranen, G. Fink, Cohesive-frictional interface model for timber-concrete contacts, International Journal of Solids and Structures. (2021) 11.

[50] L. Jin, W. Yu, X. Du, W. Yang, Meso-scale simulations of size effect on concrete dynamic splitting tensile strength: Influence of aggregate content and maximum aggregate size, Engineering Fracture Mechanics. 230 (2020) 106979. https://doi.org/10.1016/j.engfracmech.2020.106979.

[51] R. Zhang, L. Jin, M. Liu, X. Du, J. Liu, Refined modeling of the interfacial behavior between FRP bars and concrete under different loading rates, Composite Structures. 291 (2022) 115676. https://doi.org/10.1016/j.compstruct.2022.115676.

[52] F. Lebon, Contact problems with friction: models and simulations, Simulation Modelling Practice and Theory. 11 (2003) 449–463. https://doi.org/10.1016/S1569-190X(03)00060-1.

[53] L. Chiriatti, H. Mercado-Mendoza, K.L. Apedo, C. Fond, F. Feugeas, A study of bond between steel rebar and concrete under a friction-based approach, Cement and Concrete Research. 120 (2019) 132–141. https://doi.org/10.1016/j.cemconres.2019.03.019.

[54] V. Tvergaard, Cohesive zone representations of failure between elastic or rigid solids and ductile solids, Engineering Fracture Mechanics. 70 (2003) 1859–1868. https://doi.org/doi.org/10.1016/S0013-7944(03)00128-0.

[55] V. Tvergaard, Effect of fibre debonding in a whisker-reinforced metal, Materials Science and Engineering: A. 125 (1990) 203–213.

[56] RILEM TC, RC 6 Bond test for reinforcement steel. 2. Pull-out test, 1983, in: RILEM Recommendations for the Testing and Use of Constructions Materials, E & FN SPON, 1994: pp. 218–220.

[57] RILEM, Essai portant sur l’adhérence des armatures de béton–essai par traction, Matériaux et Constructions. 3 (1970) 175–178.

[58] Salome, www.salome-platform.org. https://www.salome-platform.org/.

[59] J. Mazars, Application de la mécanique de l’endommagement au comportement non linéaire et à la rupture du béton de structure, These de Docteur-Es-Sciences Presentee a l’Universite Pierre et Marie Curie-Paris. (1984).

[60] A. Hillerborg, M. Modéer, P.-E. Petersson, Analysis of crack formation and crack growth in concrete by means of fracture mechanics and finite elements, Cement and Concrete Research. 6 (1976) 773–781. https://doi.org/10.1016/0008-8846(76)90007-7.

[61] The Finite element code Cast3M, www-cast3m.cea.fr. http://www-cast3m.cea.fr/.

[62] J.G.M.V. Mier, Strain-softening of concrete under multiaxial loading conditions, PhD, Citeseer, 1984.

[63] C. Comi, U. Perego, Numerical aspects of nonlocal damage analyses, Revue Européenne Des Éléments Finis. 10 (2001) 227–242. https://doi.org/10.1080/12506559.2001.11869249.

[64] Y.-H. Lee, K.J. Willam, Anisotropic vertex plasticity formulation for concrete in-plane stress, Journal of Engineering Mechanics. 123 (1997) 714–726.

[65] G. Pijaudier-Cabot, J. Mazars, Damage models for concrete, in: Handbook of Materials Behavior, Chapter 6, Academic Press, 2001: pp. 500–512.

[66] R. Calixte, L. Jason, L. Davenne, Partial to Full Composite Action in Steel–Concrete Sandwich Beams: Development of a Modeling Strategy and Comparison to Standards, International Journal of Civil Engineering. (2022). https://doi.org/10.1007/s40999-022-00747-8.

[67] K.M. Anwar Hossain, Bond characteristics of plain and deformed bars in lightweight pumice concrete, Construction and Building Materials. 22 (2008) 1491–1499. https://doi.org/10.1016/j.conbuildmat.2007.03.025.

[68] T. Helfer, B. Michel, J.-M. Proix, M. Salvo, J. Sercombe, M. Casella, Introducing the open-source mfront code generator: Application to mechanical behaviours and material knowledge management within the PLEIADES fuel element modelling platform, Computers & Mathematics with Applications. 70 (2015) 994–1023. https://doi.org/10.1016/j.camwa.2015.06.027.

[69] J.C. Simo, T.J. Hughes, Computational inelasticity, 1st ed., Springer New York, NY, 1998. https://doi.org/10.1007/b98904.

[70] H.W. Kuhn, A.W. Tucker, Nonlinear Programming, in: Proceedings of the Second Berkeley Symposium on Mathematical Statistics and Probability, Berkeley, California, U.S.A, 1951: pp. 481–492.

[71] Y. Mi, M.A. Crisfield, G.A.O. Davies, H.B. Hellweg, Progressive Delamination Using Interface Elements, Journal of Composite Materials. 32 (1998) 1246–1272. https://doi.org/10.1177/002199839803201401.

[72] G. Alfano, M.A. Crisfield, Solution strategies for the delamination analysis based on a combination of local-control arc-length and line searches, Int. J. Numer. Meth. Engng. 58 (2003) 999–1048. https://doi.org/10.1002/nme.806.

[73] X. Wang, X. Liu, Modeling bond strength of corroded reinforcement without stirrups, Cement and Concrete Research. 34 (2004) 1331–1339.

[74] Y. Xu, W. Shen, H. Wang, Experimental study of bond behavior of reinforced concrete, Journal of Building Structures. 15 (1994) 26–37.

[75] C. La Borderie, G. Pijaudier-Cabot, Influence of the state of the stress in concrete on the behaviour of steel concrete interface, Concrete Fracture Mechanics of Structures, Colorado, USA. (1992).

[76] A.M. D'Altri, S. de Miranda, G. Castellazzi, V. Sarhosis, A 3D detailed micro-model for the in-plane and out-of-plane numerical analysis of masonry panels, Computers & Structures. 206 (2018) 18–30. https://doi.org/10.1016/j.compstruc.2018.06.007.

[77] T. Tong, S. Yuan, H. Wang, Z. Liu, J. Wang, Numerical insights on quasi-static behaviors of UHPC-NC composite members by a phase-field approach enhanced with a cohesive-frictional interface model, Composite Structures. 297 (2022) 115948. https://doi.org/10.1016/j.compstruct.2022.115948.

APPENDIX A

Tvergaard's cohesive zone model

A modified version of Tvergaard's cohesive zone model, which was initially presented in [54,55], and used in other works such as [19], is presented.

The displacement jump across the interface element $[\![u_i]\!]$ is obtained from the displacements u_i^+ and u_i^- of the points located on the top and bottom sides of the interface respectively, which are calculated with respect to a fixed coordinate system, as follows:

$$[\![u_i]\!] = u_i^+ - u_i^- \tag{A.1}$$

A non-dimensional parameter λ representing the equivalent opening of the interface is defined as follows:

$$\lambda = \sqrt{\langle [\![u_n]\!] \rangle_+^2 + \frac{[\![u_t]\!]^2 + [\![u_h]\!]^2}{\delta_s}} \tag{A.2}$$

where $[\![u_n]\!]$ is the normal displacement jump, $[\![u_t]\!]$ and $[\![u_h]\!]$ are the two tangential displacements jumps and $\langle\cdot\rangle_+$ indicates that the positive displacement jump is only considered. In addition, δ_s is the stiffness ratio defined as:

$$\delta_s = K_n/K_s \tag{A.3}$$

where K_n is the normal stiffness and K_s is the tangential stiffness in both directions.

The damage indicator $\tilde{\lambda}$ is calculated as a function of λ and of the initially assigned damage threshold λ_0 parameter:

$$\begin{cases} \tilde{\lambda} = \lambda - \lambda_0 & if\ \lambda > \lambda_0\ and\ \dot{\tilde{\lambda}} > 0 \\ \tilde{\lambda} = max\left(\widetilde{\lambda_p}, 0\right) & if\ else \end{cases} \tag{A.4}$$

where $\widetilde{\lambda_p}$ represents the previous damage indicator attained, which is initially zero, and $\dot{\tilde{\lambda}}$ is the evolution of the damage indicator, which can be calculated as $\tilde{\lambda} - \widetilde{\lambda_p}$.

In the elastic part of the model, that is when $\lambda_0 > \lambda$, the behavior is governed by normal and shear stiffness of the interfaces K_n and K_s according to the linear elastic spring model formulation:

$$\begin{pmatrix}\sigma_n\\ \sigma_t\\ \sigma_h\end{pmatrix} = \begin{pmatrix}K_n & 0 & 0\\ 0 & K_s & 0\\ 0 & 0 & K_s\end{pmatrix}\begin{pmatrix}u_n\\ u_t\\ u_h\end{pmatrix} \tag{A.5}$$

When there is no propagation of damage, or when the damage is still null, the evolution of the damage indicator $\dot{\tilde{\lambda}} = 0$ and in this case, the normal stress σ_n is calculated as follows:

$$\begin{cases}\sigma_n = \dfrac{f_t}{\tilde{\lambda} + \lambda_0} \exp\left(\dfrac{-f_t\,\tilde{\lambda}}{G_f}\right)[\![u_n]\!] & if\ [\![u_n]\!] \geq 0\\ \sigma_n = K_n[\![u_n]\!] & if\ [\![u_n]\!] < 0\end{cases} \tag{A.6}$$

where f_t is the maximum tensile strength of the interface, and G_f is the fracture energy. Note that in order to maintain continuity of the normal stress when damage is null in Eq. (A.6), the normal stiffness K_n should be initially defined as follows:

$$K_n = f_t/\lambda_0 \tag{A.7}$$

While the tangential stress σ_s in each of the two tangential directions t and h is calculated as follows:

$$\sigma_s = \frac{f_t}{\tilde{\lambda} + \lambda_0} \exp\left(\frac{-f_t\,\tilde{\lambda}}{G_f}\right)\frac{[\![u_s]\!]}{\delta_s} \tag{A.8}$$

Notice that Eqs. (A.6) and (A.8) verify Eq. (A.5) when the damage is null, i.e. $\tilde{\lambda} = 0$, which represents the elastic part of the model.

On the other hand, when $\dot{\tilde{\lambda}} > 0$, damage D_{int} propagates in the interface and it is defined as:

$$D_{int} = 1 - \exp\left(\frac{-f_t\,\tilde{\lambda}}{G_f}\right) \tag{A.9}$$

In this case, the normal stress is calculated as follows:

$$\begin{cases}\sigma_n = (1 - D_{int})\dfrac{f_t}{\lambda}[\![u_n]\!] = \dfrac{f_t}{\lambda} \exp\left(\dfrac{-f_t\,\tilde{\lambda}}{G_f}\right)[\![u_n]\!] & if\ [\![u_n]\!] \geq 0\\ \sigma_n = K_n[\![u_n]\!] & if\ [\![u_n]\!] < 0\end{cases} \tag{A.10}$$

While the tangential stress in each direction is calculated as follows:

$$\sigma_s = \frac{f_t}{\lambda} \exp\left(\frac{-f_t\,\tilde{\lambda}}{G_f}\right)\frac{[\![u_s]\!]}{\delta_s} \tag{A.11}$$

A simulation is done on one interface element connecting two blocks to each other (Figure 8). A certain normal displacement is applied either in compression or in tension and the corresponding applied force is calculated, and the results are shown in Figure A.1(a). The maximum tensile strength f_t is taken equal to 3 MPa, the fracture energy G_f is 200 N/m, the damage threshold λ_0 is 0.01 mm, while the normal stiffness K_n is calculated according to Eq. (A.5) and the shear stiffness K_s is taken equal to it, i.e. 3×10^{11} N/m^3. In addition, the tangential behaviors are shown in Figure A.1 (b), after performing several simulations on the same interface element, by imposing a certain initial tensile stress then applying a tangential displacement. One can see that the behavior is equivalent to an elastic spring model in compression, depending uniquely on the value of K_n. However, the behavior is different in tension. Before reaching the damage threshold λ_0, there is an elastic increase of the stress until reaching the peak, which is equivalent to the maximum tensile strength f_t. After reaching the peak stress, damage initiates and the normal stress decreases exponentially until reaching zero stress, and the area under the curve should be equal to the fracture energy G_f. In case of pure shear, the behavior is similar to the tensile behavior, while when a certain tensile stress is initially imposed on the interface, one can see a drop in the peak shear stress. The higher the imposed stress, the lower the peak shear stress. This is due to the propagation of damage in the interface before the application of tangential displacement for high tensile stresses and because the equivalent opening λ itself depends on the positive normal displacement according to Eq.(A.2). Thus, in case of initial compression, the corresponding shear behavior will be the same as the pure shear behavior shown regardless of the value of the compressive stress imposed.

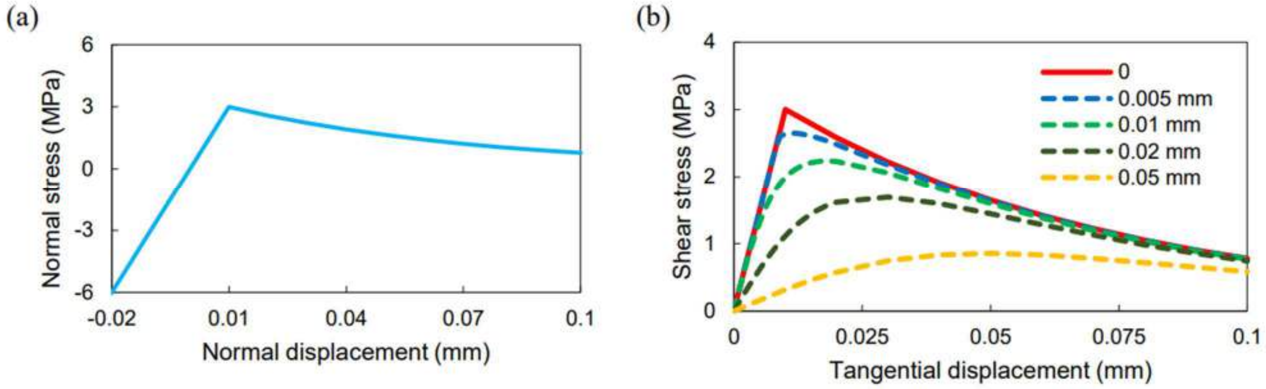

Figure A.1 Simulations performed on one-interface element using modified Tvergaard's interface model: (a) The normal stress versus the normal displacement and (b) the shear stress versus the tangential displacement under five different imposed normal displacements

APPENDIX B

Coulomb's interface model

Coulomb's interface model used in order to describe the debonding between concrete and steel bar takes into account Mohr-Coulomb's failure criterion is presented. In the elastic part of the model, the stress tensor σ of the interface element is defined according to Eq. (A.5). The interface failure occurs due to either shear or tension according to the Mohr-Coulomb's failure criterion simplified in Figure B.1.

The maximum shear stresses $\sigma_{t\ max}$ and $\sigma_{h\ max}$ in each of the two tangential directions are given by:

$$\sigma_{s\ max} = C + |\sigma_{n\ max}| \cdot \tan \emptyset \qquad \textbf{(B.1)}$$

where C is the interface's cohesion and $\emptyset$ is the interface's friction angle. $\sigma_{n\ max}$ is the maximum normal stress that is equal to the maximum tensile strength f_t , which should be predefined initially as one of the model parameters, taking into account the following constraint:

$$\sigma_{n\ max} = f_t \qquad and \qquad 0 \leq f_t \leq \frac{C}{\tan \emptyset} \qquad \textbf{(B.2)}$$

When f_t is null, the interface has no strength in tension, which means the two surfaces will instantly separate under any applied tension, resembling a contact formulation.

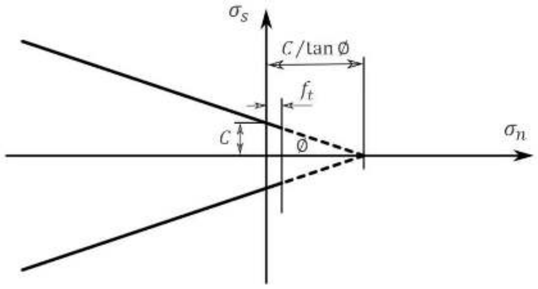

Figure B.1 Mohr-Coulomb's failure criterion for the Coulomb's interface model

The behavior in the normal direction for the Coulomb interface model described above is shown Figure B.2(a). The simulation is done also on one interface element (Figure 8). The maximum tensile strength f_t is taken equal to 3 MPa, the cohesion C is 3 MPa, the friction angle $\emptyset$ is 45°, while the normal stiffness K_n and the shear stiffness K_s are both taken equal to $10^{11}\ N/m^3$. In addition, the tangential behaviors are shown in Figure B.2(b), after performing several simulations on the same interface element, by imposing a certain compressive stress then applying a tangential displacement.

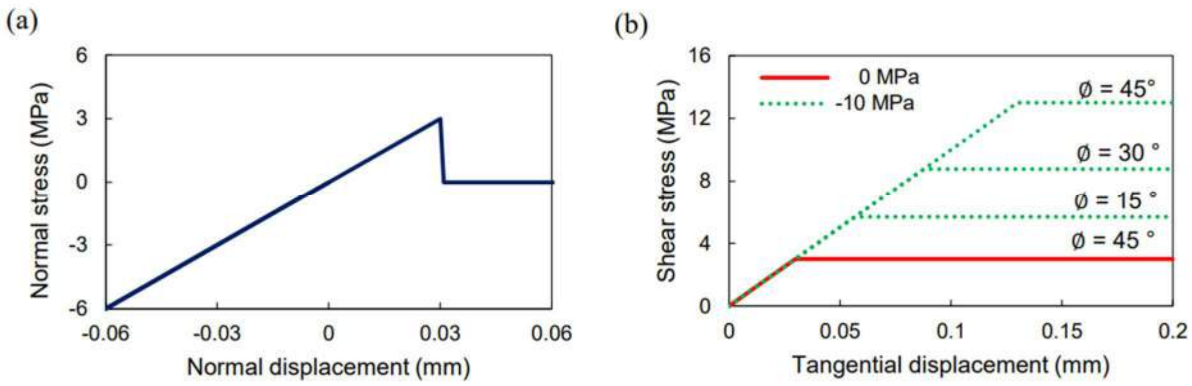

Figure B.2 Simulations performed on one-interface element using Coulomb's interface model: (a) Normal stress versus normal displacement and (b) shear stress versus tangential displacement under an imposed compressive stress and for different values of the friction angle Ø (in degrees).

One can see that the compressive behavior is equivalent to a linear elastic spring model with no peak, which is due to the non-existence of failure in compression in this model and due to elastic behavior clearly stated in Eq. (A.5). Thus, the compressive behavior depends uniquely on the value of the normal stiffness K_n. On the other hand, the behavior in tension does not only depend on the normal stiffness K_n, but also on the maximum tensile strength f_t. One can see that the elastic behavior is similar to that in compression, which depends similarly on K_n. In addition, separation failure is captured when the normal stress reaches the maximum normal strength f_t, after which the normal stress flips to null instantly. However, the tangential behavior is different from the exhibited behavior in the normal direction. This behavior consists of two parts: a linear increase in stress followed by a constant stress. The first part is the elastic part, which depends uniquely on the shear stiffness K_s. This behavior ceases when the maximum shear stress $\sigma_{s\,max}$ expressed in Eq. (B.1) is reached, maintaining a constant stress. This second part depends on the maximum compressive stress $\sigma_{n\,max}$, the cohesion C and the friction angle $\emptyset$. The residual stress will always be equal to the peak stress, without any change in the stress during the post peak behavior.

Generation

3D pullout samples

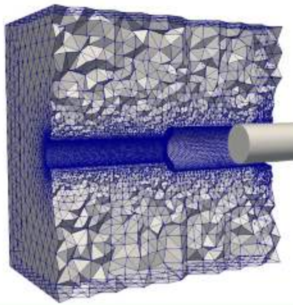

Smooth bar

Ribbed bar

Problem

Tvergaard's cohesive zone model

Coulomb's interface model

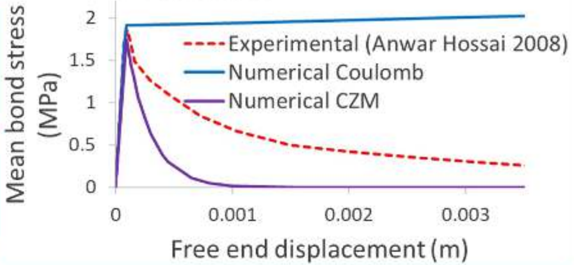

Not possible to reproduce the behavior

Proposed Solution

Frictional cohesive zone model

Tvergaard's Damage + Friction

$$\sigma = (1 - D)\sigma^u + D\sigma^d$$

Verification

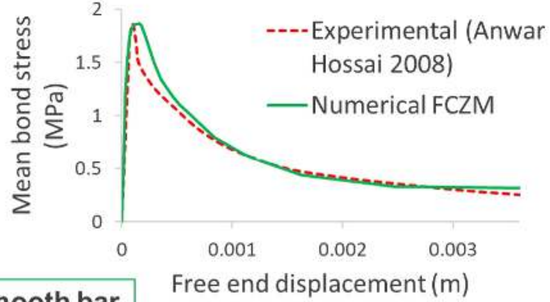

Smooth bar

Ribbed bar

Verification

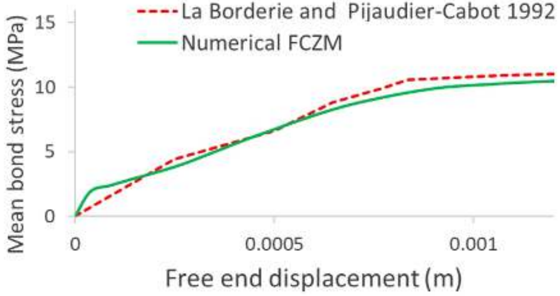

Good agreement with experimental results

All three principle stresses